Unterschrift BetreuerIn

TECHNISCHE UNIVERSITÄT WIEN
Vienna University of Technology

DIPLOMARBEIT

Analysis and Estimation of Uncertainties in $H \to \tau\tau$ and $Z \to \tau\tau$ analyses with the CMS experiment

ausgeführt am Institut für Hochenergiephysik (HEPHY)
der Österreichischen Akademie der Wissenschaften

unter der Leitung von
Univ.Prof. Dipl.-Phys. Dr.rer.nat. Jochen Schieck
und
Dr. Martin Flechl
(als verantwortlich mitwirkender Assistent)

durch

David Dorffner
00926631

Wien, 11. Dezember 2017

Unterschrift StudentIn

Analysis and Estimation of Uncertainties in the $H \to \tau\tau$ and $Z \to \tau\tau$ decay channels with the CMS experiment

Abstract

The Large Hadron Collider Run II provides with 13 TeV almost double the center of mass energy than the previous run. A major focus at the Large Hadron Collider lies in the measurement of the properties of the so-called "Higgs boson". After discovering it in 2012 the Large Hadron Collider Run II now offers the possibility to solidify this model for further research.

Since the Higgs boson cannot be detected directly, it is necessary to analyse the end products of its decay channels. An essential tool is the simulation of proton proton collisions to generate events, which offer a good basis to test mathematical models before being applied to the real life data delivered by the Compact Muon Solenoid detector at the Large Hadron Collider. This simulation is based on parton distribution functions, describing the impulse share of each parton (quarks or gluons) in a proton. This thesis is dedicated to the question which effects small variations in the parton distribution functions have on the results of the simulation of observables. The $H \to \tau\tau$ and $Z \to \tau\tau$ decay channels are subject to scrutiny. This was done by determining the parton distribution function uncertainties of simulated data (using MadGraph and POWHEG event generators) and exploring their effects on observables such as the visible mass m_{vis}, as recommended by the PDF4LHC group.

This thesis concludes that the resulting uncertainties are generally in the range of 0.18% to 1.3%. Concerning the estimated uncertainties of each sample, parton distribution function uncertainties might play a slightly more significant role in Drell-Yan processes than in Higgs boson production like vector boson fusion or gluon fusion. In contrast stand the uncertainties deriving from scale variation. These turn out significantly higher for gluon gluon fusion, were in the most extreme case values of up to 12% are estimated. This suggests that scale uncertainties have a larger impact on events than parton dis-

tribution function uncertainties. Ratio plots visually show that the parton distribution function uncertainties are constantly smaller than the statistical error of the distribution itself.

Contents

1. Introduction

The CMS group of the LHC is investigating the properties of the Higgs boson, after its existence was proven in 2012. Now, after the facilities at the LHC were updated, a center-of-mass energy of 13 TeV is available.
Since the Higgs boson cannot be measured directly, researchers must investigate its decay channels to make estimations about the behaviour of its decay products. This thesis is dedicated to the analysis of said decay channels and also offers a look at the $Z \to \tau\tau$ channel, which has the same final state.
The first part of this thesis is dedicated to the theoretical background of the search for the Higgs boson. Section 2 will give a brief introduction into the standard model and the mathematical basis for the Higgs boson, followed by an overview over the main Higgs production processes and Higgs channels. This thesis will concentrate on the vector boson Fusion (VBF) and gluon gluon Fusion (ggF) production of the Higgs boson. Also included is a section about the experimental hardware at the LHC and its detector CMS, which explains the different components necessary to detect particles of any kind such as for example leptons and hadronic showers (section 4).
The centrepiece of this thesis is the estimation of the actual uncertainty estimation based on simulated data. Key question is the determination of uncertainties under variation of the Parton Distribution Functions (PDFs).
Section 5 will further explain the procedure behind the uncertainties estimation, especially the mathematical tools, that allow to calculate said uncertainties. Simulated data processed by the MadGraph and POWHEG event generators provide the basis for this analysis. For each sample various histograms are produced to visualize the change of observables (e.g. visible mass m_{vis}) under PDF variation as well as to demonstrate the influence on the acceptance of selection cuts.
The results are presented in sections 6 and 7. In the process the focus lies on the $H \to \tau\tau$ decay. Section 8 gives an interpretation of the results and this thesis is completed with conclusions in section 9.

2. Electroweak Theory and the Higgs mechanism

The Standard Model (SM) is one of the most successful and most experimentally challenged theories in modern physics. It describes three of the four fundamental forces – the electromagnetic, weak and strong interaction – and classifies the elementary particles into six quarks, up (u), down (d), charm (c), strange (s), top (t) and bottom (b) quark and six leptons, the electron (e), the muon (μ), the τ-lepton and their corresponding neutrinos (ν_e, ν_μ and ν_τ) . Both the quarks and the leptons occur in generations (e.g. up and down quark, electron and electron neutrino and so on). Furthermore four bosons exist, which serve as mediators for the forces, the gluon (g), the photon (γ) and the massive $W^{\pm}$ and Z bosons. At last the SM also contains a scalar boson with a spin of zero, the so-called Higgs boson (H), which was discovered in 2012.

The SM describes the interaction of matter as the exchange of particles as a force carrier. The basic principle of the SM is the assumption about certain mathematical symmetries, the so-called gauge symmetries U(1), SU(2) and SU(3). The SM postulates that these symmetries must not be infringed, even when the at any point in space a transformation (like a rotation) is executed (local gauge invariance). To achieve this, the Lagrange density, the function describing the energy of the system, needs to be modified. This leads to the introduction of a new vector field, which serves as a mediator field, meaning it represents particles (bosons) which exchange force between two matter particles.
For example the postulation of gauge invariance concerning U(1) symmetry leads to the introduction of a new vector field A_μ, which can be interpreted as a field of photons, which serve as exchange particles for the electromagnetic force between two charged particles. Similar assumptions can be made for the strong interaction (SU(3)) and weak

Quarks	u	c	t	
	d	s	b	
Leptons	e	μ	τ	
	ν_e	ν_μ	ν_τ	
Gauge Bosons	g	γ	$W^{+/-}$	Z
Scalar Boson	H			

Table 1: The elementary particles of the standard model categorized into quarks, leptons, gauge bosons, and the scalar boson. The three columns in the quark and lepton section represent the particles, which are grouped into generations.

interaction (SU(2)).
The SM is not only able to describe many observed phenomena, but in the past could successfully predict the existence of many unknown particles, like for example the top-quark and the tau-neutrino. Still many questions remain unanswered. Aside from the fact, that it does not include the theory of gravity, the SM cannot explain certain aspects such as the mass spectrum of neutrinos (since they are considered massless in the SM, contrary to recent experimental evidence) or why particles are divided into three generations. One major flaw while developing the SM was the fact that initially the SM described the vector bosons $W^{\pm}$ and Z^0 as massless, when in fact they are one of the most massive particles. The introduction of a mass term

$$m^2 A^{\mu} A_{\mu} \tag{1}$$

with A_{μ} representing the massive boson vector field and m the bosons mass, would violate the gauge invariance of the Lagrangian. Under these circumstances the three massive gauge bosons, W^+, W^- and Z^0, would be massless. A mechanism to describe massive bosons and the mass of fermions was necessary.
This could be resolved by the so-called Higgs mechanism.

2.1. Higgs mechanism

The solution to this problem was the concept of spontaneous symmetry breaking, where a non-zero vacuum has a different symmetry than the Lagrangian. Define a complex scalar field

$$\phi = \frac{\phi_1 + i\phi_2}{\sqrt{2}} \tag{2}$$

with ϕ_1 being the real part and ϕ_2 the imaginary part of the field. The scalar field must be invariant under global $U(1)$ (a compact Lie group) transformation, meaning that the underlying physics must not change under rotation of the field

$$\phi \rightarrow e^{i\alpha}\phi \tag{3}$$

around an arbitrary phase angle α. This is represented in a Lagrange density of the following form

$$\mathcal{L} = (\partial^{\mu}\phi^*)(\partial_{\mu}\phi) + U \tag{4}$$

with the potential U being

$$U = \mu^2\phi^*\phi + \lambda^2(\phi^*\phi)^2 \tag{5}$$

with μ and λ being constants defining the size of the Potential. A potential of this shape is also referred to as a "mexican hat potential". It is remarkable, that the ground state is not well defined any more because any value along the circle

$$\phi_1^2 + \phi_2^2 = \frac{\mu^2}{\lambda^2} \tag{6}$$

represents a valid ground state (red circle in fig. 1). This is the so-called Higgs field.

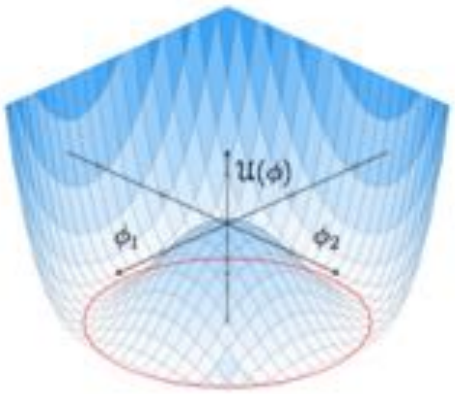

Figure 1: A graph of the Potenial U as a function of the real part ϕ_1 and imaginary part ϕ_2 of the scalar field ϕ. The red circle represents all possible values, which can be chosen as a ground state (*source: [1], page 12*).

Usually any choice of a ground state would immediately break the symmetry of the theory because as a result one value would be distinguished from the other possible values. Since the invariance under U(1) transformation was postulated beforehand, any value can be a possible ground state. Considering that, one might choose an arbitrary value and expand around the ground state in terms of perturbation theory. The field can now be rewritten as

$$\phi = \frac{1}{\sqrt{2}} \left[\frac{\mu}{\lambda} + \eta + i\xi \right] \tag{7}$$

with

$$\eta = \phi_1 - \frac{\mu}{\lambda}, \quad \xi = \phi_2 \tag{8}$$

being excitations in the field. When substituted into the initial Lagrangian (4) the result is a real, massive scalar field η with mass $m_\eta = \sqrt{2}\mu$ and a massless scalar field ξ, which, considering the Goldstone theorem, appears whenever a global symmetry is broken. Such a boson has not been observed. Three independent groups, among them Higgs, introduced a mechanism in 1964, which eliminated the need for a Goldstone boson [2].

The basic idea is to consider the breaking of symmetry, but postulating local gauge invariance, compared to the global invariance above. This means that the Lagrangian from eq. (4) must be invariant to transformations of the form

$$\phi \to e^{i\alpha(x)}\phi. \tag{9}$$

Important hereby is the lokal dependence of the phase angle ($\alpha \to \alpha(x)$). That requires to define the covariant derivative

$$D_\mu = \partial_\mu - igA_\mu \tag{10}$$

with A_μ being a massless scalar vector field, which transforms accordingly to our condition for invariance under local $U(1)$ transformation. When inserting the covariant derivative in (4), the Lagrangian takes the form

$$\mathcal{L} = [(\partial\mu - igA\mu)\phi^*][(\partial_\mu - igA_\mu)\phi] + \mu^2\phi^*\phi - \lambda^2(\phi^*\phi)^2 - \frac{1}{4}F^{\mu\nu}F_{\mu\nu} \tag{11}$$

The last term describes the dynamics of A_μ with $F_{\mu\nu}$ being the field tensor for A_μ, and g is a coupling constant. Again we choose the same ground state as previously and expand around it in terms of η and ξ. The Lagrange density develops to

$$\begin{aligned} \mathcal{L} = &\left[\frac{1}{2}(\partial^\mu\eta)(\partial_\mu\eta) - \mu^2\eta^2\right] + \left[\frac{1}{2}(\partial^\mu\xi)(\partial_\mu\xi)\right] + \\ &+ \left[-\frac{1}{4}F^{\mu\nu}F_{\mu\nu} + \frac{1}{2}\left(g\frac{\mu}{\lambda}\right)^2 A^\mu A_\mu\right] - i\left(g\frac{\mu}{\lambda}\right)(\partial^\mu\xi)A_\mu + \\ &+ coupling\ terms + constant\ terms \end{aligned} \tag{12}$$

The boson ξ still exists and some terms seem to indicate that it couples to A_μ, which now has acquired a mass $m_A = g\frac{\mu}{\lambda}$. One can turn back to local gauge invariance and rewrite the field in dependency of new fields h and θ, with h being the radial mode and θ being the azimuthal mode of the field ϕ:

$$\phi = \frac{1}{\sqrt{2}}\left(\frac{\mu}{\lambda} + h(x)\right)e^{i\frac{\lambda}{\mu}\theta(x)} \tag{13}$$

Now a particular gauge can be chosen that the azimuthal mode θ can be eliminated and

is absorbed by the gauge field A_μ. Finally the Lagrange density modifies to

$$\begin{aligned} \mathcal{L} = &\left[\frac{1}{2}(\partial^\mu h)(\partial_\mu h) - \mu^2 h^2\right] + \\ &+ \left[-\frac{1}{4}F^{\mu\nu}F_{\mu\nu} + \frac{1}{2}\left(g\frac{\mu}{\lambda}\right)^2 A^\mu A_\mu\right] - i\left(g\frac{\mu}{\lambda}\right)(\partial^\mu \xi)A_\mu + \\ &+ coupling\ terms + constant\ terms \end{aligned} \tag{14}$$

The Goldstone boson ξ has been dissolved into the massive gauge field A_μ which represents the massive gauge bosons. The last remaining variable is the scalar Higgs field h, the quantum of which is the Higgs boson.
To recap, by reformulating the Lagrange density around a non-zero ground state and removing the Goldstone boson via a gauge transformation, a massive gauge field could be generated. This is the so-called Higgs mechanism for U(1). For the full theory also SU(2) symmetry breaking need to be addressed.

2.2. Electroweak unification

Building on the works of Higgs and Glashow, Salam and Weinberg developed the theory of electroweak unification (EWT), postulating not only the invariance of a system under U(1) transformation, but also under SU(2) transformation, the symmetry describing the mathematical space of isospin. Demanding gauge invariance under SU(2) transformation results in three massless vector boson fields W_i^μ (i = 1, 2, 3) which all together can be written as the field $\boldsymbol{W}^\mu$. In analogy to the electromagnetic interaction U(1) gauge invariance introduces the massless vector boson field B^μ. With these new fields the Lagrange density can be modified to:

$$\begin{aligned} \mathcal{L}_{EW} = &-\frac{1}{4}\boldsymbol{W}_{\mu\nu}\boldsymbol{W}^{\mu\nu} - \frac{1}{4}B_{\mu\nu}B^{\mu\nu} + \\ &+ \bar{f_L}\gamma^\mu\left(i\partial_\mu - g\frac{1}{2}\sigma\boldsymbol{W}_\mu - g'\frac{Y}{2}B_\mu\right)f_L + \\ &+ \bar{f_R}\gamma^\mu\left(i\partial_\mu - g'\frac{Y}{2}B_\mu\right)f_R \end{aligned} \tag{15}$$

where $\boldsymbol{W}_{\mu\nu}$ and $B_{\mu\nu}$ are field tensors to the vector fields $\boldsymbol{W}_\mu$ and B_μ, σ represents the Pauli matrices, which are required for transformations (rotations) in the isospin space and g and g' are coupling parameters. The first two terms describe the dynamics of the free vector fields $\boldsymbol{W}_\mu$ and B_μ. Term 3 and 4 stem from the Lagrange density of the dirac equation for quarks and leptons. The split into two parts comes from the fact that

EWT groups together left and right-handed leptons and quarks (a property also called chirality, which derives of the spin direction compared to the direction of momentum of the particle) into the spinors (complex vectors with spin components) f_L and f_R
In analogy to section 2.1 four real scalar fields combined to a complex doublet are introduced:

$$\phi = \frac{1}{\sqrt{2}} \begin{pmatrix} \phi_1 + i\phi_2 \\ \phi_3 + i\phi_4 \end{pmatrix}. \tag{16}$$

In order to generate mass $\boldsymbol{W}_\mu$ and B_μ need to couple to ϕ by adding the term

$$\mathcal{L}_{Higgs} = \left| \left(i\partial_\mu - g\frac{1}{2}\sigma \boldsymbol{W}_\mu - g'\frac{Y}{2}B_\mu \right) \phi \right|^2 + U(\phi) \tag{17}$$

to the Lagrange density of the system. $U(\phi)$ is the potential from (5).
As described in section 2.1, a ground state must be chosen in order to rewrite ϕ as

$$\phi = \frac{1}{\sqrt{2}} \begin{pmatrix} 0 \\ v + h(x) \end{pmatrix} \tag{18}$$

with $v = \frac{\mu}{\lambda}$ depending on the size of the Higgs potential.
When inserting (18) into eq. (17) $\mathcal{L}_{Higgs}$ can be rewritten as

$$\begin{aligned} \mathcal{L}_{Higgs} = \frac{1}{2}\left(\partial^\mu h\right)\left(\partial_\mu h\right) - \mu^2 h^2 + \\ + \frac{1}{4}v^2 g^2 W^{\mu +} W^-_\mu + \\ + \frac{1}{8}v^2 \left(g^2 + g'^2\right) Z^\mu Z_\mu + \\ + A^\mu A_\mu + \\ + couplingterms + constantterms \end{aligned} \tag{19}$$

with the new fields

$$W^\pm_\mu = \frac{W^1_\mu + iW^2_\mu}{\sqrt{2}} \qquad Z_\mu = \frac{gW^3_\mu - g'B_\mu}{\sqrt{g^2 g'^2}} \qquad A_\mu = \frac{g'W^3_\mu - gB_\mu}{\sqrt{g^2 g'^2}}. \tag{20}$$

These fields represent the massive $W^\pm$ and Z bosons and the photon (vector field A_μ), which does not couple to the Higgs field and therefore is massless. Also a scalar Higgs boson h is involved, which has the mass $m = \sqrt{\mu}$ (apparent from the second term of $\mathcal{L}_{Higgs}$, which constitutes a mass term). This coincides with the observations made in experiments.

3. Higgs phenomenology

3.1. Production

Among others the Standard Model predicts four major processes in which a Higgs boson is produced at the LHC. The most common one is gluon-gluon fusion, $gg \to H + X$. The second most common production process is the so-called Vector Boson Fusion production mode, $gg \to ggH + X$. Those two production modes are the relevant ones in this thesis. Apart from the above-mentioned processes, there is the so-called Associated Production involving $W^{\pm}$ or Z^0 Bosons, $gg \to VH + X$, where V stands for said Bosons. At last, with a considerably smaller production rate, there is Associated Production with a top and an anti-top quark [3].

3.1.1. Gluon Fusion

As previously mentioned, gluon-gluon fusion (ggF) is the most commonly occurring production mode. Two gluons form a Higgs boson through a quark loop. Even though every quark is a viable candidate, in practice this production mode proceeds through a top quark loop, because of its remarkable mass (it is the most heavy elementary particle observed so far) [4].

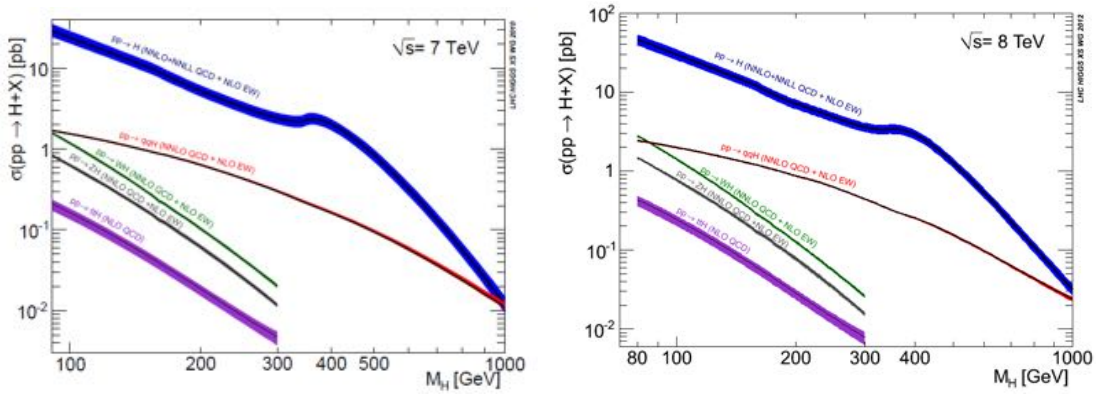

(a) (b)

Figure 2: Predicted Higgs production cross section with center of mass energies of 7 TeV (a) and 8 TeV (b) for different production modes [5].

The cross sections are calculated at next-to-next-to-leading-logarithmic (NNLL) accuracy in Quantumchromodynamic (QCD) and next-to-leading-order (NLO) accuracy in Electroweak Theory (EWK). Here terms like NNLL, NLO or NNLO describe degrees

of accuracy in the calculations (more on this topic in section 5). The Higgs production cross sections at the LHC are shown in Figure 2 as a function of the Higgs bosons mass (as the mass had to be determined experimentally and was not known before the discovery of the Higgs boson in 2012). The predicted cross sections for a 125 GeV Higgs boson produced by ggF are about 20 pb with an uncertainty of about 15% at 8 TeV center-of-mass energy at the LHC [4].

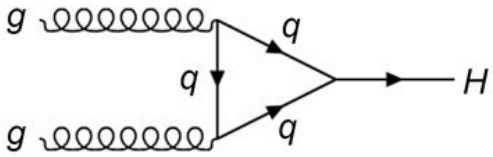

Figure 3: Feynman diagramm of Gluon Fusion. Two gluons form a Higgs boson through a (top) quark loop.

3.1.2. Vector Boson Fusion

The second most often occurring production mode at LHC is the Vector Boson Fusion (VBF). A pair of quarks emit W or a Z bosons, which combine to form a Higgs boson. VBF events are easy to distinguish from other events, because of two remaining hadronic jets in forward direction [1]. Cross sections are calculated at NNLO accuracy in Quantumchromodynamics (QCD) and NLO accuracy in Electroweak theory (EWT). This results in predicted cross sections of about 1.6 pb with an uncertainty of about 3% (concerning a 125 GeV Higgs boson at 8 TeV center-of-mass energy at the LHC).

3.1.3. $W^{\pm}/Z^0$ Associated Production

Apart from ggF and VBF there are also the Associated Production modes (VH). Two quarks can create a W or a Z boson, which therefore can emit a Higgs boson. That means this process leaves a remaining W or a Z boson.
Estimations for the cross section of Associated Production (NNLO accuracy in QCD and NLO accuracy in EWT) are down to 0.7(0.4) pb with an uncertainty of about 4%(5%)

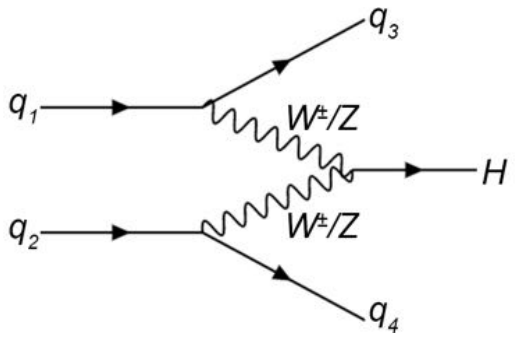

Figure 4: Feynman diagramm of Vector Boson Fusion. Two quarks respectively emit W or Z bosons, which combine to a Higgs boson.

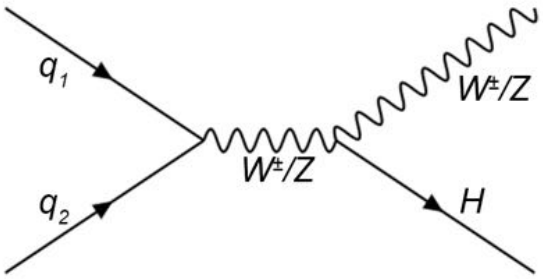

Figure 5: Feynman diagramm of $W^{\pm}/Z^0$ Associated Production. Two quarks create a W or Z boson, which emits a Higgs boson.

3.1.4. $t\bar{t}$ Associated Production

Creating a Higgs boson with a top quark pair might seem reasonable because of its high mass, which would make it easier to decay into the compared to other particles heavy Higgs boson, but since consequentially it decays in a decisively short period of time, it makes the entire process rather unlikely.
The process starts with two gluons decaying into a top-antitop pair ($t\bar{t}$), as well as a top and antitop quark annihilating and emitting a Higgs boson.

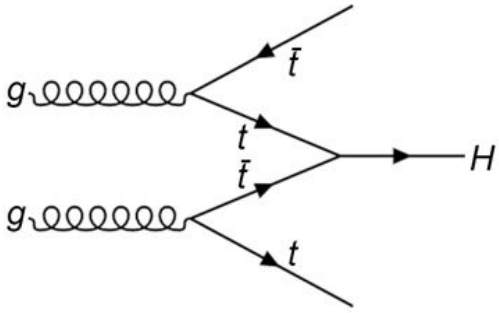

Figure 6: Feynman diagram of $t\bar{t}$ Associated Production. Two gluons decay into $t\bar{t}$ pairs. A t and $\bar{t}$ then combine to a Higgs boson.

3.2. Decay

Properties, that influence decay of elementary particles, such as half life, decay product, etc., heavily rely on the particle's mass. Pre-LHC experiments could narrow the bandwith in which the mass of a potential Higgs boson lies down to an area between 114 GeV and 200 GeV [1] before it was discovered, that the Higgs boson actually had a mass of 125 GeV. This opened a variety of possible decay channels. It even made it possible for the Higgs boson to decay to more massive particles like hadrons [3].
Since the findings of 2012 at the LHC suggest that the Higgs particle has a mass of 125 GeV and a resulting half life of $1.6 \times 10^{-22} s$, the SM predicts that it most likely decays into a $b\bar{b}$ quark pair with a rate of 56,1%. Less frequent, but still the second most occurring fermion decay is the $H \to \tau\tau$ decay, which is subject to investigation in this thesis.
Also decay into a massive gauge boson is likely, such as a W boson (23,1%) or a Z boson (2,9%), which furthermore decay into quark pairs or leptons (electrons, muons). Although the W boson decay is more likely to happen, the Z boson decay channel is of more interest, since its following decay into leptons is easier to detect and distinguished from background than the W bosons decay into a bottom quark pair [6]. Also massless gauge particles are possible, even tough this process requires an intermediate loop of virtual top or bottom quarks. Again, even though the decay into gluons is more likely, photons as a decay product are easier and more precise to detect and therefore more relevant to experimental research [7].

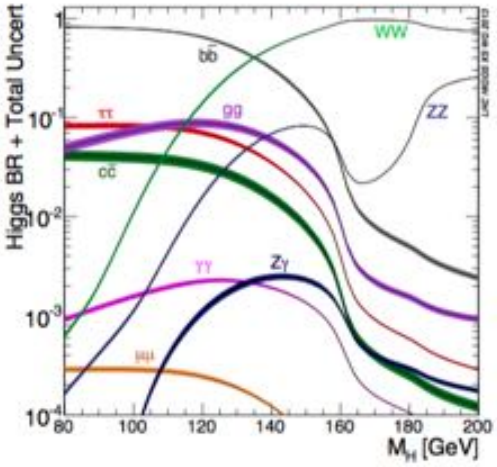

Figure 7: Propabilities for the occurrence of certain Higgs decay modes in dependency of its possible mass [5].

4. Experimental background

An important tool for a physicist to broaden the understanding about fundamental workings of the nature of elementary particles is a collider experiment. Beams of particles are accelerated to very high kinetic energies and collided against either a fixed target of sample particles or against each other. Thereby a reaction occurs, in which the projectile particles can be transformed into new particles. By measuring properties like energy and momentum of the end products, one might make valuable assumptions about the underlying physics.
The biggest experiment facility in this regard up to date is the LHC, located at the research organisation CERN in Geneva, Switzerland [8]. With energies of 13 TeV, physicists strive to answer some of the current big questions engaging the scientific community. Besides the search for the Higgs boson physicists hope to learn about phenomena like "Dark Energy" or Supersymmetry (SUSY).

4.1. LHC

The LHC is a circular particle accelerator where two beams of protons or heavy ions are accelerated in opposite directions and are collided at the four detectors CMS, ATLAS, ALICE and LHCb. It is a ring of superconducting magnets built into a tunnel system with a circumference of about 27 km, under the French-Swiss border. Each beam could reach 4 TeV in 2012, but after a 2-year construction period in 2015 and 2016 ener-

gies of 6.5 TeV per beam were achieved. That means that the protons move at about 99.999999% of the speed of light. It takes a proton 90 µs to travel once through the ring, which adds up to about 11 000 revolutions per second.
The LHC consists of 1232 dipol magnets, which in a set of two coils (for the two beams) create a magnetic field of up to 8.3 T. These are supposed to force the charged particles on their orbit. 400 quadrupole magnets are responsible to focus the beams. They are superconducting magnets, the whole system is cooled down to 1.9 K.
To achieve acceleration the LHC uses high frequency resonators. 16 superconducting radio frequency cavities are partitioned along the ring, in which the protons are steadily accelerated with wave frequency of 400 Mhz. The protons are not continuously aligned, but are separated in up to 2808 bunches per beam. Every bunch can hold about 10^{11} protons and is 25 ns apart from the others.
An important factor in particle physics is the luminosity of the scatter or collider experiment. It indicates the number of particles per unit of time. At the LHC peaking luminosities of up to 10^{34} $cm^{-2}s^{-1}$ were reached [9].

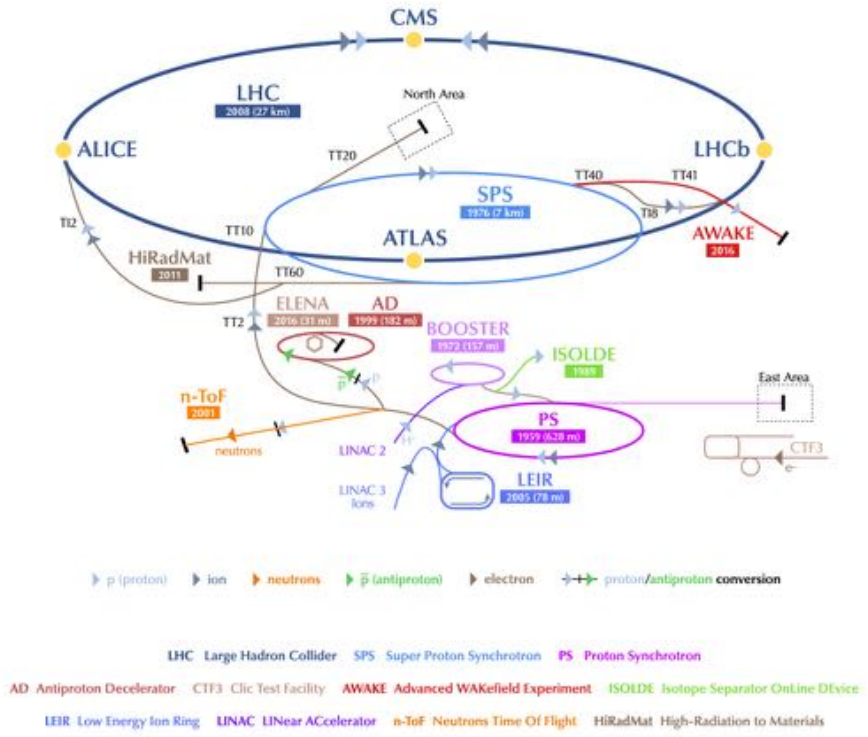

Figure 8: A map of the LHC complex, with the location of its detectors (the major four being CMS, ATLAS, ALICE and LHCb) (*source: [10] and* `https://cds.cern.ch/record/1621894`).

4.2. CMS

CMS is one of the four detectors at the LHC and one of the two major all-purpose ones (besides ATLAS). It stands for Compact Muon Solenoid and gets its name from being designed to especially detect Muons [1]. It is 13 m long and 15 m in diameter. Its centerpiece is the 6 m wide superconducting solenoid magnet. With a magnetic field of 3.8 T it was designed to curve the path of charged particles emerging from the collisions, especially the hard-to-detect muons, to later determine their momentum. Most of the detector instruments are located inside the solenoid. [11]
As a reference for orientation a cartesian coordinate system can be laid on the cross section of the detector, with the origin being at the point of collision, but also polar coordinates, with Φ being the transverse angle and θ the angle between the path of the emerging particle and the beam. However most of the time the so-called pseudorapidity

$$\eta = -\ln\left(\tan\left(\frac{\theta}{2}\right)\right) \tag{21}$$

is used as a measure for localization in the detector. In the course of this paper the pseudorapidity will also be used (a depiction of the magnitude of η can be seen in figure 9.
The detector can be roughly divided into the barrel ($|\eta| < 1.5$) and the end caps ($1.5 < |\eta| < 3$).

4.2.1. Tracking System

The tracking system is the first layer of the barrel and located right next to the point of collision, covering a range of $|\eta| < 2.5$. Its purpose is to track the paths of particles going through. Since the magnetic field of the solenoid bends the path, the momentum of the particles can be determined. The transverse momentum p_T can be calculated as

$$p_T = qrB \tag{22}$$

with q being the charge of the particle, r being the track radius and B the magnetic field of the solenoid. It is mainly made of silicon detectors in two components. The inner pixel detector spans from 4.4 to 10.2 cm from the collision point. Covering a surface of one square meter it contains 68 million pixels to guarantee high resolution. The outer Silicon Strip detector covers 1.1 m. It consists of 9.8 million silicon strips, which, spread out, would range over an area of 195 m^2 [12]. Silicon was the choice of material, since it handles the intense flux of particles and radiation (Bremsstrahlung etc.), while

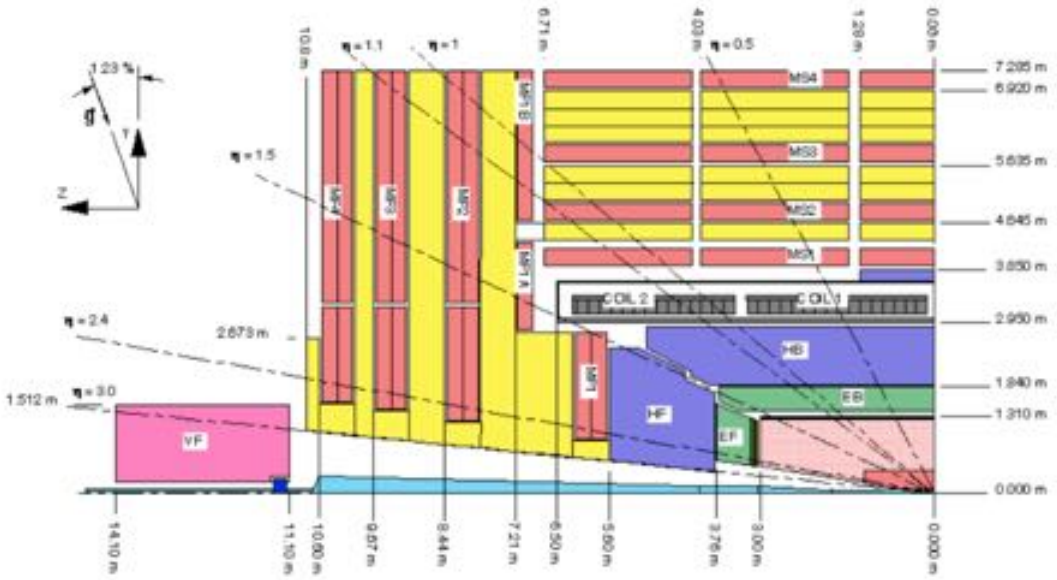

Figure 9: Cross section through the CMS detector and its components. It also shows the different values for the pseudorapidity η (*source: [12], page 29 and* `http://www-hep.phys.cmu.edu/cms/PICT_ARCH/cms_side_view.gif`).

still requiring minimal material to function. That ensures that the detector material can detect the particle, without interfering too much and at worst causing multiple scattering, photon conversion or nuclear interaction, which dampens the resolution of the detector.

As a charged particle travels through the silicon in the detector, it creates free electrons and holes. The free electrons flow off over electrodes, where its current can be measured. Therefore the current is proportional to the number of particles traveling through the detector. This results in high resolutions, with an accuracy of up to 10 μm [12].

4.2.2. Electromagnetic Calorimeter

The Electromagnetic Calorimeter (ECAL) measures the energy of electromagnetic particles such as photons and electrons (as well as positrons). Its main constituents are lead tungstate crystals ($PbWO_4$). $PbWO_4$ is optically clear and has a high density of 8.29 g/cm^{-3}. This is required to produce scintillation, which then again can be measured as a signal by photodiodes. [11]

ECAL is allocated in the barrel ($|\eta| < 1.479$) right after the tracking system and in the end caps ($1.479 < |\eta| < 2.5$). The crystals are arranged in a tight matrix, separated

by carbon fibres to isolate each one of them optically. Each crystal has a length of 230 mm and a diameter of 22 mm, which is roughly the same as the Molier Radius (radius of the cylinder containing 90% of an electromagnetic particles' average shower energy). Altogether the barrel part of ECAL consists of 61,000 crystals, while the end caps consist of 7324 crystals each.
For extra spatial resolution the ECAL also has so-called preshower detectors in front of the end caps. This is a sampling calorimeter, which is built in two layers. The first, a lead radiator, creates an electromagnetic shower when particles pass through. Its deposited energy then can be measured by the second layer, a silicon strip detector. The preshower detector has the purpose to distinguish between neutral pions and photons. Also it identifies the difference between high and low energy photons, with high energy photons being of huge significance, since they are often an indicator for interesting physical events.
The resolution of ECAL depends on several aspects such as lateral containment, photostatistics, electronic noise or event pileup noise. Pileup is the effect of bunch crossings producing separate events, which are measured as noise that can be troublesome to the actually significant events. On average, ECAL has a good reolution of 1% for a 40 GeV energy deposit.

4.2.3. Hadron Calorimeter

Between ECAL and the solenoid sits the Hadronic Calorimeter (HCAL). It measures the energy of hadronic showers, the so-called jets. It is essential to determine the missing transverse energy (MET), energy that is carried away by neutrinos, which can not be detected at CMS.
HCAL is divided into three parts: the barrel (HB) at $|\eta| < 1.3$, the end caps (HE) at $1.3 < |\eta| < 3$ and the Forward HCAL which range over an area of $3 < |\eta| < 5.2$ [11]. HB consist of 36 brass wedges alternating with plastic scintillators. In this case brass is suitable, because it is non magnetic and has a short interaction length (length on which energy of incoming particle decreases to 1/e %). HE has a similar build up. As a charged particle travels through brass, it reacts with its nuclei and emits light. This light can be detected by photo diodes.
The Forward HCAL is made of steel and measures Cherenkov radiation, which is emitted when a particle travels through a medium faster than light does. This coherently different layout allows for better seperation of particles in forward direction, since naturally this area is significantly congested.

4.2.4. Muon System

The predominant part of the CMS detector is the Muon System, which lies around the solenoid and makes up the outer layer of the whole complex. This is owed to the fact that muons can travel rather unaffected through matter for several meters. Therefore the Muon System had to be designed in the impeccable size of ten times the interaction length of the muon with matter. It consist of three different kinds of detectors: drift tubes (DT), cathode strip chambers (CSC) and resistive plate chambers (RPC). The whole system is surrounded by a 1.8 T return field.
Drift tubes are filled with gas, which is ionized by high energy particles traveling through. With an array of electrodes, where the ionized current flows off, a precise localization of the particles path is enabled. DTs are built in the barrel and are aligned in concentric cylinders around the beam line.
The CSC system consists of a total of 486 cathode strip chambers and is located in the end caps ($1.2 < |\eta| < 2.4$). CSC is also based on the principle of measuring current from ionizing gas, but differ in the layout of the electrodes, since the cathode are conductor strips instead of wires.
RPCs are implemented to tag the time of muon events faster than 25 ns (the time between two beam crossings), to guarantee precise mapping of the measured muon to its original event. This is essential for the Trigger, the component of the CMS, that presorts the recorded data and eliminates insignificant events, to sort out the relevant ones. It consists of two metal plates separated by gas. Compared to the other components DT and CSC, it provides fast measurement but lacks the spatial resolution the others have. It is built between DT and CSC in the barrel as well as in the end caps.
The resolution can vary depending on the location in the detector, with 1.3% and 2.0% in the barrel and up to 6% in the end cap [11].

5. $H \to \tau\tau$ and $Z \to \tau\tau$ Analysis

This thesis estimates uncertainties of simulation due to PDF and scale uncertainties. This section will describe the preparation leading up to the actual analysis.

5.1. Sample preparation

Every sample consists of an collection of particle collisions called "events". Every event describes the process of two protons interacting with each other and the often resulting particles created directly after the proton collision, which interact with each other to form the final particles [13]. In simulations used to examine proton collisions these processes are based on perturbation theory and the non-perturbative PDFs using Monte Carlo simulation [14]. Simulation starts with event generators. The three main event generators used for the production of the samples in this thesis are Pythia, MadGraph and POWHEG. All are accessible over the CMSSW software framework of the CMS experiment.
This thesis examines three different simulated processes: a Higgs boson produced by either VBF or ggF and decays into two τ leptons, or a Z boson is created (by a Drell-Yan process) and decays into two τ leptons at leading order or next-to-leading order, referring to the order used in the perturbation theory describing the underlying processes. Every event contains a variety of data describing the process such as for example the number of constituents involved in the event, the number of jets produced and their momentum and mass. A first preselection is run through the events to reject events or categorize events into three decay channels based on which kind of articles are reconstructed in the event:

- $\mu\tau$ channel: One τ lepton decays into a μ lepton and neutrinos, the other τ lepton decays hadronically.
- $e\tau$ channel: One τ lepton decays into an electron and neutrinos, the other τ lepton decays hadronically.
- $\tau\tau$ channel: Both τ leptons decay hadronically.

Analysis in this paper also determines, if the particles involved are correctly reconstructed (see section 6.1 and 6.1).
Table 2 shows the total number of events generated per sample.

Sample	Total number of events
Drell-Yan LO	9 004 240
Drell-Yan NLO	19 259 560
VBF	1 496 072
ggF	1 499 028

Table 2: Total number of events simulated for each sample.

As the thesis examines the $H \to \tau\tau$ and $Z \to \tau\tau$ decay channels, it is essential to pick out certain events, when jets can be identified as the τ particles of aforementioned decay channels, as well as their leptonic decay products, the muon and electron, which are detectable (the τ particle has a very short half-life of around $3 \times 10^{-13} s$, therefore it is impossible to directly measure it in the detector). Unfortunately muons and electrons are also by-products in other processes and can overlap other events in form of pileup.

5.1.1. Parton model

The concept of "partons" refers to the constituents of hadrons, such as baryons like protons and neutrons, but also mesons like pions and kaons: the quarks and gluons. The term derived from the first theories and algorithms used to describe and calculate particle showers emerging from collision experiments, roughly a decade before Quantumchromodynamics was introduced and partons were identified as quarks and gluons. Even though outdated, the parton model still serves as a viable approximation for scatter processes in high energy physics.
The model explains hadrons as an accumulation of point-like particles, the partons. To determine cross sections for the collision of two hadrons the notion is used that these partons undergo scattering processes to perturbatively calculate the cross sections. The scattering particles thereby only see the hadrons as a whole and only at higher energies can resolve the partons as well. The so-called parton distribution functions (PDF) are fundamental and serve as a weight function for calculations. They are a probability density function of the longitudinal momentum share of the partons inside the particle [7].

5.1.2. Generating PDF and scale variation weights

An essential tool to determine PDF and scale variation uncertainties is the reweighting of events. Weights are created, which can be applied to events and represent the variation of the PDFs or scales that were used to generate these events [15]. When generating a sample, for each event a set of N_{mem} (in the case of this thesis $N_{mem} = 100$) PDF

weights are simultaneously created, representing different variations of the PDFs within their uncertainties. In addition, nine scale variation weights are created.

PDF weights describe the effects of varying the parton distribution functions on generating events. Due to systematic errors, PDF parameters are varied around a certain error margin to determine the propagation of uncertainties. A more detailed description can be found in reference [16].

Scale variation weights describe the effects of varying the factorization and renormalization scale on generating events.
Calculating the cross sections of proton-proton collisions, which primarily involve inelastic scattering processes, is not possible solely with perturbation theory [17]. Therefore, the calculation is split into one part based on perturbation theory and one experimentally determined part, which will turn out to be the PDFs. This convolution is used to calculate the possibilities of the outcome of collisions. The factorization theorem is defined in the following matrix calculation:

$$W^{\mu\nu} = \sum_a \int_x^1 \frac{d\xi}{\xi} f_{a/A}(\xi, \mu_F) H_a^{\mu\nu}(\xi, \mu, \alpha_s(\mu_F)) + additional\ terms. \tag{23}$$

Eq. 23 is a convolution of the PDF $f_{a/A}$, describing the probability of a parton a (gluon, quark, etc.) in proton A carrying the fraction ξ to $\xi + d\xi$ of the protons momentum x, with the tensor $H_a^{\mu\nu}$, representing the part of the equation which can be calculated by means of perturbation theory. $H_a^{\mu\nu}$ is dependent on the parameter of the strong interaction α_s and the factorization scale μ_F, which will become relevant.
These two part of the equation, the PDF $f_{a/A}$ and are also called "hard" (for the perturbative part) and "soft" (for the non-perturbative part, the PDFs) QCD processes [1]. The quantity μ_F is used to scale the balance between both parts of the factorization [18]. The second important scale is the renormalization scale μ_R. It is used when higher orders in perturbative calculations – which would add diverging energies to the system – are cancelled out by applying corrections to the mass and coupling constant. By choosing a convenient renormalization scale the effect of those higher orders can be minimized [19].

Reweighting is an essential tool to display different outcomes due to PDF or scale variation, without needing to compute the whole process for each variation from scratch. This is possible because the cross section calculation can be rewritten as linear combi-

nations of scale- or PDF-dependent terms with coefficients that are independent of scale and PDFs [20]:

$$d\sigma = f_1(x_1, \mu_F) f_2(x_2, \mu_F) g_s(\mu_R) w d\chi \tag{24}$$

with f_1 and f_2 being the PDFs for the first and the second proton of the collision, x_i their momentum fraction, μ_F the chosen factorization scale and $g_s(\mu_R)$ a renormalization scale-dependent factor. $d\chi$ represents all integration variables. The factor w is the coefficient containing all scale- and PDF independent factors, which can be easily computed once for all additional variations.
When integrating eq. 24 one obtains a set of N events

$$\{x_{1,i}, x_{2,i}, \Xi_i\}_{i=1}^{N} \tag{25}$$

with the calculated cross sections Ξ_i. Now when choosing alternative scales and PDFs, f_i', μ_R', and μ_F', one can simply reweight Ξ_i by using

$$\Xi_i \to \Xi_i \mathcal{R}_i. \tag{26}$$

with the weight $\mathcal{R}_i$ which can be calculated solely by using the initial and the new PDFs and scales:

$$\mathcal{R}_i = \frac{f_1'(x_{1,i}, \mu_F') f_2'(x_{2,i}, \mu_F') g_s(\mu_R')}{f_1(x_{1,i}, \mu_F) f_2(x_{2,i}, \mu_F) g_s(\mu_R)}. \tag{27}$$

It is now possible to obtain any PDF or scale variations by simply computing the corresponding $\mathcal{R}_i$ [20].

5.2. Uncertainties Analysis

Four major samples are subject to investigation:

- $Z \to \tau\tau$ Drell-Yan production generated with MadGraph at leading order.
- $Z \to \tau\tau$ Drell-Yan production at next-to-leading order using the POWHEG event generator.
- $H \to \tau\tau$ where the Higgs boson H is produced through VBF.
- $H \to \tau\tau$ where the Higgs boson H is produced through ggF.

Every event is represented by an array of values, the entries of which contain all important physical quantities and observables relevant to this particular event. This includes items like the momentum of the particles involved, the number of jets produced in the

collision, the visible mass m_{vis} (referring to the visible mass of a Z/H candidate, which can be calculated by adding the 4-vectors of all visible decay products such as electrons and muons and determining the mass of the resulting 4-vector), and many other variables vital to the depiction of an event.
Also included with every event and essential to the following uncertainty calculations are sets of weights, which refer to the variation of the PDFs used in the simulation of the events.
There are four different kinds of weights:

- **PDF weights:** A set of a hundred values referring to the weight of the particular event in any observable distribution regarding variation of the PDFs.
- **Scale weights:** A set of nine weights, necessary to compute the scale uncertainties of a certain distribution (also see section 5.2.3).
- α_s **weights:** Two weights that correspond to the usage of the maximally or minimally value allowed within uncertainties for α_s, the coupling of the strong interaction (see also section 5.2.4).

These weights are used to weight every event when filling a histogram or counting events. Every entry i represents the i^{th} variation of the PDFs. Two different graphs will become important for the course of all uncertainty analysis in the upcoming chapters and will be created with every new sample and decay channel:

The **cuts** graph documents the efficiency of a preselection, a number of cuts based on predefined conditions (can be looked up in sections 6.1 and 7.1 for each sample). It visualizes the decrease of the number of events which fulfil each criteria. In the case of the PDF uncertainties all hundred variations are shown in the same plot, thereby allowing to study the uncertainties of each result. These uncertainties will be determined by calculating the standard deviation (SD) or 68% confidence level (CL). This step will be explained even further in the following sections.
The value on the y-axis refers to the efficiencies. It represents the percentage of how many events from the initial total number fulfil each criterion up to a certain cut.
The efficiency for every histogram bin is calculated by the number of events per bin divided by the total number of events, which were generated during the simulation.

The $\mathbf{m_{vis}}$ histogram illustrates the distribution of events for the observable of the visible mass. The distributions for all 100 sets of PDF weights are shown in the same plot. In

anology to the cuts histogram, the occurring PDF uncertainties can be calculated using SD or CL.

5.2.1. Standard Deviation

Since in this thesis the generation is based on the PDF4LHC recommendation for uncertainty estimation [16], the PDF uncertainties can be calculated by two different measures. The first and most common one is the computation of the standard deviation for the PDF uncertainty $\delta^{pdf}\sigma$:

$$\delta^{pdf}\sigma = \sqrt{\frac{1}{N_{mem}-1}\sum_{k=1}^{N_{mem}}\left(\sigma^{(k)} - \langle\sigma\rangle\right)^2} \tag{28}$$

whereas N_{mem} is the total number of PDF sets, which in this case equals $N_{mem} = 100$ (since PDF4LHC15_mc offers a variety of sets with different numbers of Eigenvectors) [16].
$\sigma^{(k)}$ in this case equals the calculated value of the observable of PDF set with index k (observables such as m_{vis}, p_T, etc.).
$\langle\sigma\rangle$ refers to the mean value, which conventionally computes as

$$\langle\sigma\rangle = \frac{1}{N_{mem}-1}\sum_{k=1}^{N_{mem}}\sigma^{(k)}. \tag{29}$$

In many cases the mean value breaks down to $\langle\sigma\rangle \approx \sigma^{(0)}$, but for the calculations mentioned in this thesis, which uses the Monte Carlo PDF sets, it is recommended to calculate $\langle\sigma\rangle$ as done in eq. (29).

5.2.2. Confidence Level

The second possibility to determine PDF uncertainties is by the 68% confidence level. First of all, the calculated $N_{mem} = 100$ values of the observable $\sigma^{(k)}$ need to be rearranged in order of increasing value, that means

$$\sigma^{(0)} \leq \sigma^{(1)} \leq \sigma^{(3)} \leq ... \leq \sigma^{(N_{mem})}. \tag{30}$$

The 68% CL interval can now be easily determined by using the values of the PDF set number (16) and (84) (which hold 68% of all PDF sets).

$$\delta^{pdf}\sigma = \frac{\sigma^{(84)} - \sigma^{(16)}}{2}. \tag{31}$$

The confidence level is a more suitable measure for the uncertainty, e.g. when statistical outliers occur. Especially in the case of a non-Gaussian distribution it is recommended to use the midpoint of the 68% interval [16].

$$\langle\sigma\rangle = \frac{\sigma^{(84)} + \sigma^{(16)}}{2}. \tag{32}$$

as the mean value $\langle\sigma\rangle$ for the Standard Deviation eq. (28) instead of eq. (29) to guarantee a more precise result when analysing PDF uncertainties.
In case of large discrepancy between the two methods, standard deviation and confidence level, it is recommended to adopt the CL results instead of SD results [16].

5.2.3. Scale Uncertainties

The simulation delivers an additional set of weights, the scale weights, which describe variation the of the renormalization and factorization scales. The weights consist of nine entries per event. Each entry stands for a certain scale variation:

0. μ_R and μ_F both nominal value
1. μ_R nominal and μ_F twice the nominal value
2. μ_R nominal and μ_F half the nominal value
3. μ_R twice and μ_F nominal value
4. μ_R and μ_F both twice the nominal value
5. μ_R twice and μ_F half the nominal value
6. μ_R half and μ_F nominal value
7. μ_R thalf and $\mu_F$twice the nominal value
8. μ_R and μ_F both half the nominal value

Entry number 0 refers to the nominal scale, entry indices 5 and 7 are dropped, since they show unphysical behaviour because of anti-correlated variations.
The remaining weight entries (indices $1, 2, 3, 4, 6, 8$) are then used to vary the observable and compute the envelope of the observables distribution. The envelope visualizes the scattering of the varied values around the mean value of the unweighted observable.
The deviation of the maximum and the minimum value of the envelope from the mean value are calculated and added to the SD and CL uncertainty calculations.

5.2.4. Combined PDF+α_s uncertainties

The following formulas only apply to the next-to-leading-order simulations, which were only used in the analysis of the $Z \to \tau\tau$ decay channel (more on this in section 6.3).
This not only includes the uncertainty derived from the variation of the parton distribution functions but also of the variation of α_s, which determines and parametrizes the strength of the strong interaction between color-charged particles, such as quarks and gluons.
Experimentally the value of α_s has been determined to be

$$\alpha_s = 0.1180 \pm 0.0015. \tag{33}$$

at the 68% confidence level. PDF4LHC delivers a set of weights for the maximum value of $\alpha_s = 0.1195$ and minimum value $\alpha_s = 0.1165$. After the observables are varied with these two sets of weights the α_s-uncertainty $\delta^{\alpha_s}\sigma$ respectively can be computed as following:

$$\delta^{\alpha_s}\sigma = \frac{\sigma(\alpha_s = 0.1195) - \sigma(\alpha_s = 0.1165)}{2} \tag{34}$$

In combination with the PDF uncertainties calculated according to eq. (28) and/or eq. (31) the combined PDF+α_s uncertainties $\delta^{PDF+\alpha_s}\sigma$ can be computed as

$$\delta^{PDF+\alpha_s}\sigma = \sqrt{(\delta^{PDF}\sigma)^2 + (\delta^{\alpha_s}\sigma)^2}. \tag{35}$$

6. Uncertainties in the $Z \to \tau\tau$ decay mode

This section analyses two samples which both simulate the $Z \to \tau\tau$ decay with the Z boson being created by the means of a Drell-Yan-process, a scattering process evoked by quark-antiquark annihilation. The differences between the two samples are the event generators used to produce them and the perturbation theory accuracy with which they are produced. The first was produced with the MadGraph event generator at leading order and the second one was produced with the POWHEG event generator at next-to-leading order.

6.1. Preselection

The initial data created by simulation was already reduced during the sample preparation (section 5.1), by only considering events which involve τ leptons, now even further cuts are applied to the remaining data.
Each event needs to pass the following cuts:

0. **Lepton veto**: A discriminator against electrons and muons reconstructed as a (hadronically decayed) τ lepton.
1. **Isolation 1**: Demanding an isolated first lepton (electron, muon or hadronic τ decay).
2. **Isolation 2**: Demanding an isolated hadronic τ decay (very tight isolation for events of the $\tau\tau$ channel and tight isolation for $\mu\tau$ and $e\tau$).
3. **Third lepton veto**: The event must not contain a third reconstructed lepton.
4. **Dimuon/electron veto**: No second electron or muon reconstructed.
5. **Number of jets**: Event should contain two or more jets with transverse momenta $p_T > 25$ GeV.
6. **nbtag**: Number of jets tagged as initiated by a B meson.
7. **Transverse mass**: Transverse mass of the W candidate built from a light lepton and E_T^{miss} must be smaller than 40 GeV.
8. **Decay mode**: Demanding a reconstructed decay mode compatible with a hadronic τ lepton decay.

6.2. Results for the Drell-Yan sample at leading order

The first sample was simulated with the event generator MadGraph. It describes the Drell-Yan production of a Z boson, which decays into two τ leptons. A total of 9 004 240 events were generated. The preselection is applied on each of the three decay channels ($\mu\tau$, $e\tau$ and $\tau\tau$) and each includes a graph of the PDF uncertainties (section 5.2) to visualize the effects of the PDF variation on every single cut.
Afterwards the focus turns to the visible mass m_{vis}, which is plotted into a histogram to determine the effects of the PDF uncertainties on m_{vis}.

6.2.1. Cuts and Uncertainties

Table 3 shows the efficiency after every cut.

	$\mu\tau$	$e\tau$	$\tau\tau$
0	0.13	0.24	0.013
1	0.13	0.24	0.013
2	0.12	0.22	0.01
3	0.06	0.12	0.004
4	0.003	0.003	0.00012
5	0.0025	0.0029	0.0001
6	0.0025	0.0029	0.0001
7	0.0025	0.0027	0.0001
8	0.0024	0.0026	0.00009

Table 3: Efficiencies (number of events passed divided by the initial total number of events) after every cut for every decay channel.

The uncertainties can be viewed in the figure 10. It shows the interval in which the values calculated vary. Standard deviation and confidence level result in very small values with 0.93 - 0.95% in SD. The scale uncertainties have more inconsistent values around 0.3 to 0.6% and have their peaks at the 3rd and 4th cut with up to 1%. Incidentally these are the cuts with the most decrease in efficiency.
Only the $\tau\tau$ channel seems to differ from the others, since its uncertainties result in slightly higher values with greater divergence between cuts.

Figure 10 shows a side-by-side comparison of the cut histograms and their corresponding uncertainty calculation. It is a visualization of the behaviour, especially around cut no. 3 and 4. A further discussion of these calculations can be found in section 8.

6.2.2. m_{vis} and Uncertainties

Only events with m_{vis} between 60 GeV and 120 GeV were considered when the histogram was generated. The histogram was divided into bins of 10 GeV each.

For better visualization the uncertainties can be seen next to its m_{vis} histogram in figure 11. The $\tau\tau$ decay channel stands out here, since its uncertainty values are significantly higher than in the $\mu\tau$ or $e\tau$ decay channel. This is likely due to the higher statistical uncertainties in this channel.
In general the standard deviation and confidence level repeatedly show no particular pattern, especially when significant changes in efficiency occur. The scale uncertainties, on the other hand, show a more random behaviour in areas with substantially lower efficiencies.

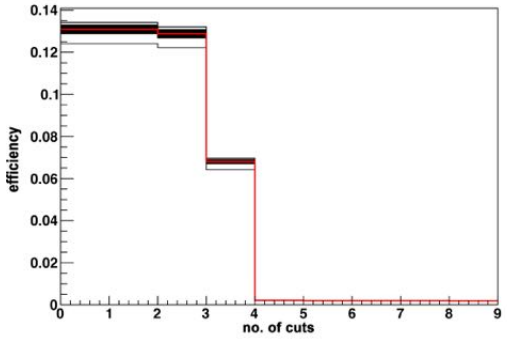

(a) cuts in $\mu\tau$ decay channel

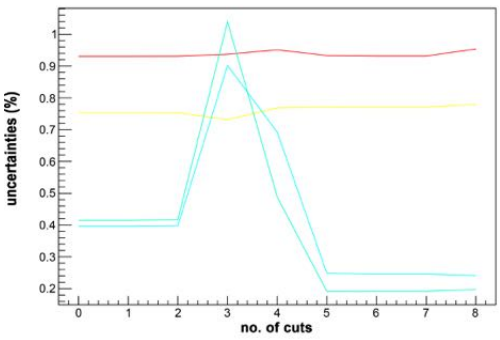

(b) $\mu\tau$ decay channel uncertainties

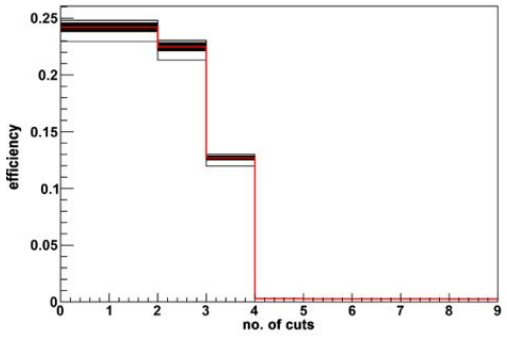

(c) cuts in $e\tau$ decay channel

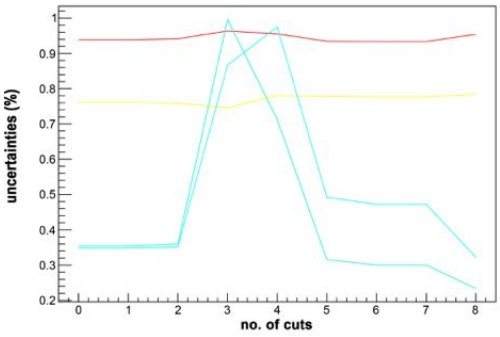

(d) $e\tau$ decay channel uncertainties

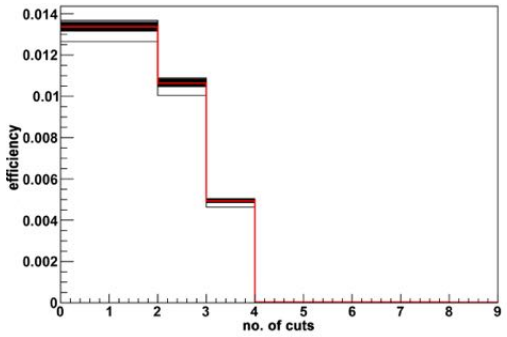

(e) cuts in $\tau\tau$ decay channel

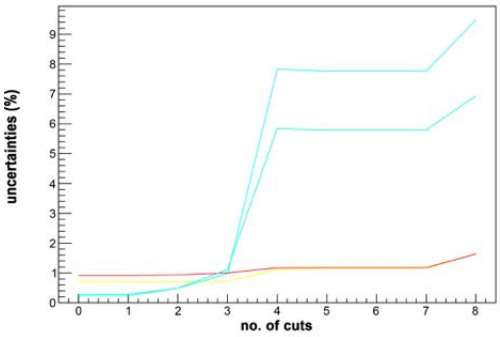

(f) $\tau\tau$ decay channel uncertainties

Figure 10: Drell-Yan LO sample cuts for every decay channel. All 100 sets are plotted on top of each other (the central value is highlighted in red). *Left column*: histogram of efficiency development after every cut. *Right column*: corresponding uncertainties(red: SD; yellow: CL; cyan/teal: scale min/scale max).

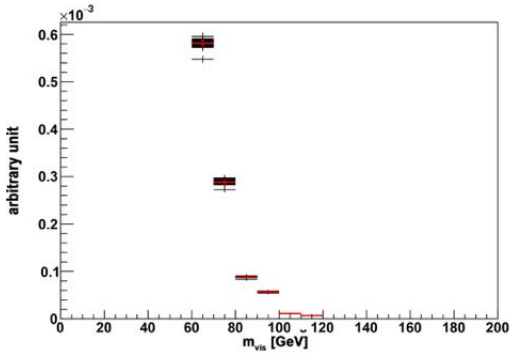

(a) m_{vis} in $\mu\tau$ channel

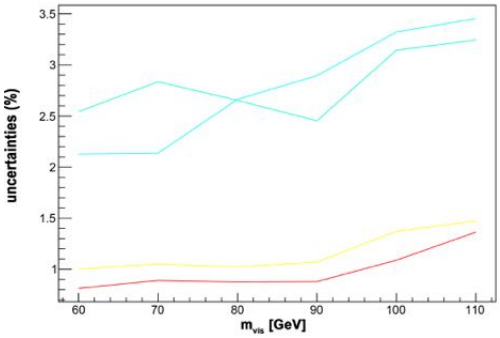

(b) m_{vis} uncertainties in $\mu\tau$ channel

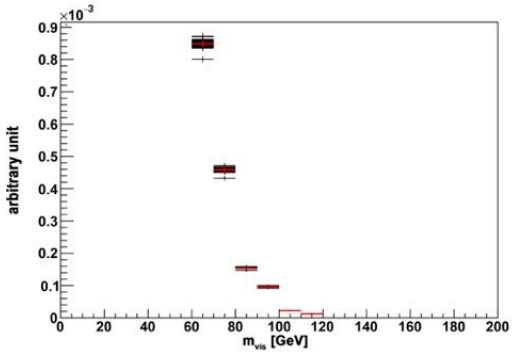

(c) m_{vis} in $e\tau$ channel

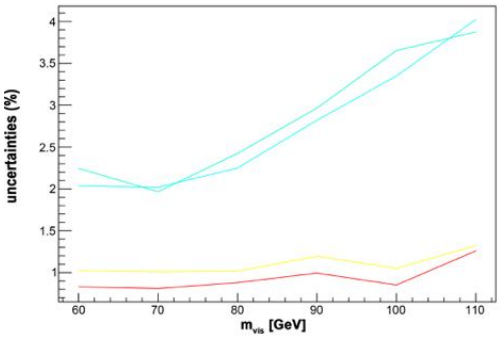

(d) m_{vis} uncertainties in $e\tau$ channel

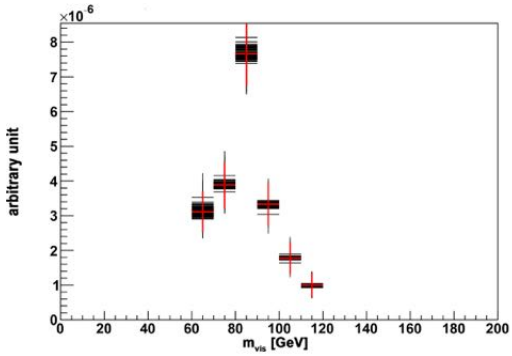

(e) m_{vis} in $\tau\tau$ channel

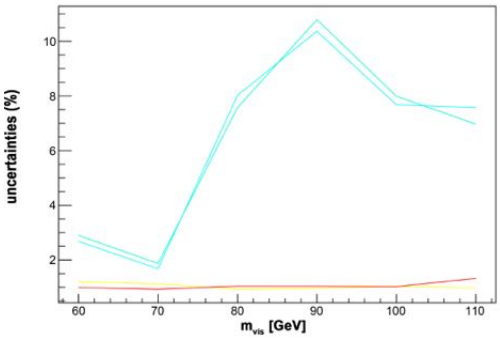

(f) m_{vis} in $\tau\tau$ channel

Figure 11: Drell-Yan LO m_{vis} distribution for every decay channel. All 100 sets are plotted on top of each other (the central value is highlighted in red). *Left column*: histogram of the number of events after the cuts divided by the total number of initial events plotted against m_{vis} in GeV. *Right column*: corresponding uncertainties(red: SD; yellow: CL; cyan/teal: scale min/scale max).

6.3. Results for the Drell-Yan sample in next-to-leading-order

The following sample describes the Drell-Yan production of a Z boson. As opposed to the previous sample this one was created at next-to-leading order using the event generator POWHEG. The analysis procedure resembles the analysis in the preceding section. All 100 sets of PDF variation are plotted into the same histogram. Subsequently the uncertainties are computed and available in side-by-side comparisons at the end of this section. The visible mass is also determined together with the corresponding uncertainties. Lastly a closer look is given at the α_s uncertainties which appear when the simulation is computed both with the minimum and maximum value for α_s, the coupling of the strong force.

6.3.1. Cuts and Uncertainties

The efficiencies can be extracted from table 4.

	$\mu\tau$	$e\tau$	$\tau\tau$
0	0.13	0.24	0.13
1	0.13	0.24	0.13
2	0.13	0.23	0.017
3	0.069	0.12	0.005
4	0.0022	0.0031	0.001
5	0.002	0.003	0.001
6	0.002	0.0029	0.00098
7	0.0019	0.0028	0.00093
8	0.0018	0.0025	0.00088

Table 4: Efficiencies after every cut for every decay channel.

The uncertainties are generally lower than the Drell-Yan LO values. Otherwise they show the same behaviour throughout the preselection.
In this sample the focus also lies on the α_s uncertainty. Remarkable are the very low values of 0.02 - 0.07% of the α_s uncertainties compared to the PDF (0.5 - 0.7%) or scale uncertainties (0.3 - 0.8%), which signals, that they are more significant when estimating uncertainties than α_s uncertainties are (more on the interpretation of the result in section 8). The graphs of the α_s uncertainty for all decay channels are displayed in figure 14.

The plotted graphs and histograms can be viewed in figure 12.

6.3.2. m_{vis} and Uncertainties

The uncertainties start off very low for the $\mu\tau$ and $e\tau$ itself but are comparatively high for the $\tau\tau$ decay channel. This also manifests in the α_s uncertainties, which were computed for this sample. The m_{vis} uncertainties are displayed on the m_{vis} figure on the right-hand side (figure 13b, 13d and 13f), the α_s uncertainties in figure 14.

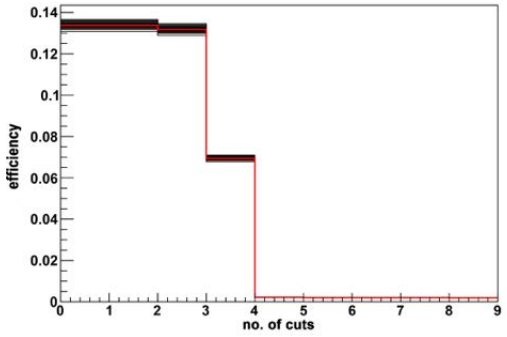

(a) cuts in $\mu\tau$ decay channel

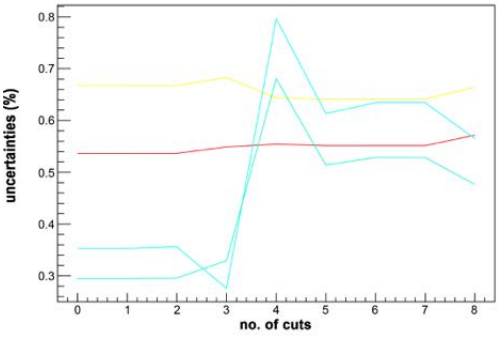

(b) $\mu\tau$ decay channel uncertainties

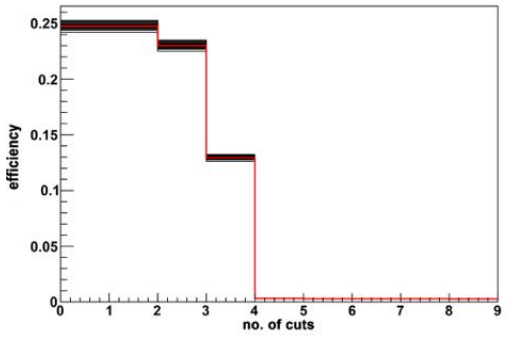

(c) cuts in $e\tau$ decay channel

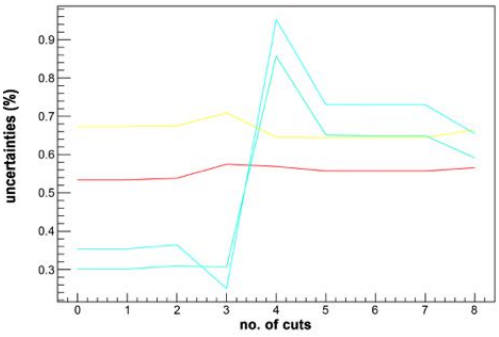

(d) $e\tau$ decay channel uncertainties

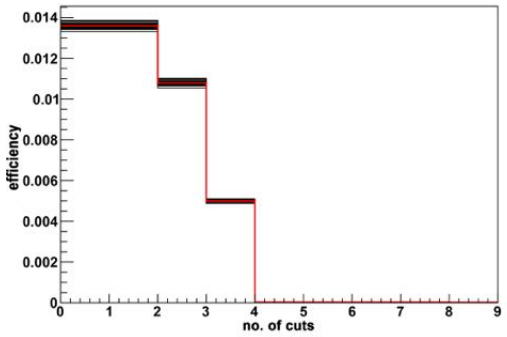

(e) cuts in $\mu\tau$ decay channel

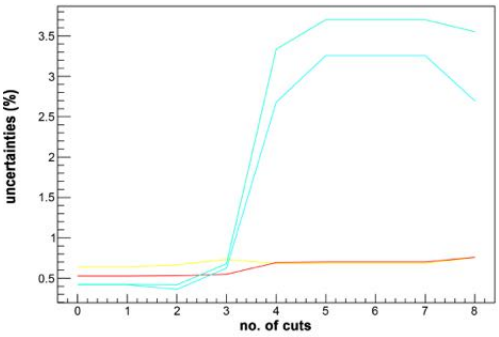

(f) $\tau\tau$ decay channel uncertainties

Figure 12: Drell-Yan NLO sample cuts for every decay channel. All 100 sets are plotted on top of each other (the central value is highlighted in red). *Left column*: histogram of efficiency development after every cut. *Right column*: corresponding uncertainties(red: SD: yellow: CL; cyan/teal: scale min/scale max).

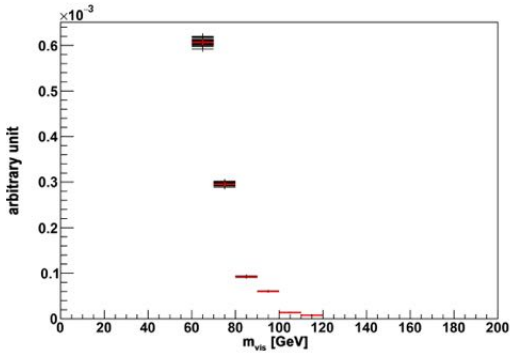

(a) m_{vis} in $\mu\tau$ channel

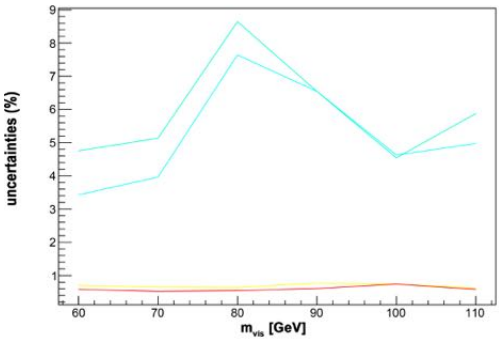

(b) m_{vis} uncertainties in $\mu\tau$ channel

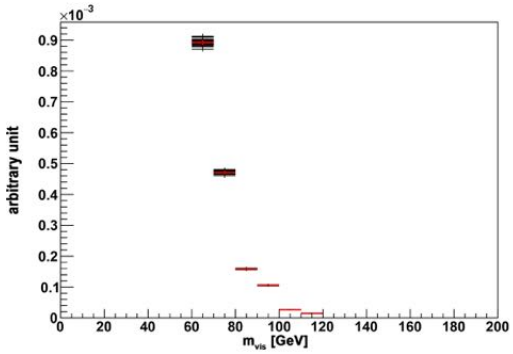

(c) m_{vis} in $e\tau$ channel

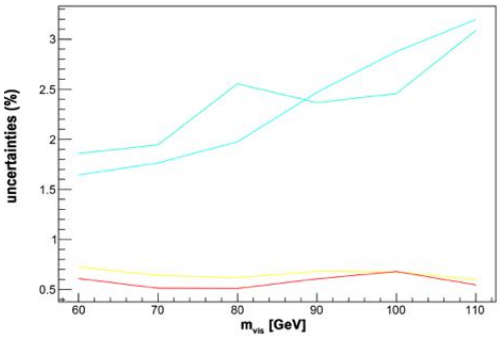

(d) m_{vis} uncertainties in $e\tau$ channel

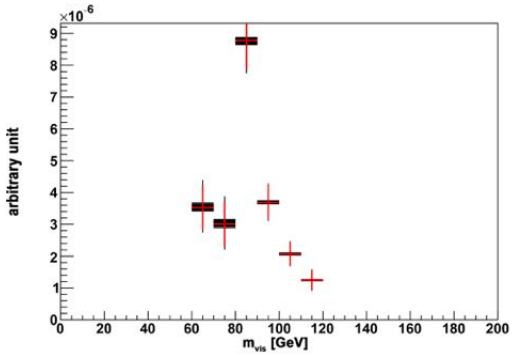

(e) m_{vis} in $\tau\tau$ channel

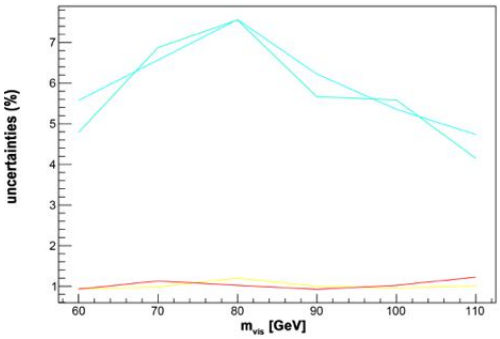

(f) m_{vis} uncertainties in $\tau\tau$ channel

Figure 13: Drell-Yan NLO m_{vis} distribution for every decay channel. All 100 sets are plotted on top of each other (the central value is highlighted in red). *Left column*: histogram of the number of events after the cuts divided by the total number of initial events plotted against m_{vis} in GeV. *Right column*: corresponding uncertainties(red: SD; yellow: CL; cyan/teal: scale min/scale max).

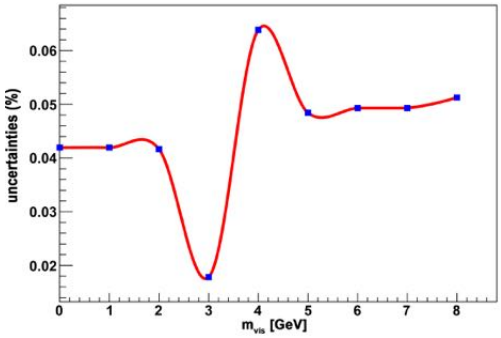

(a) cuts α_s uncertainty $\mu\tau$ channel

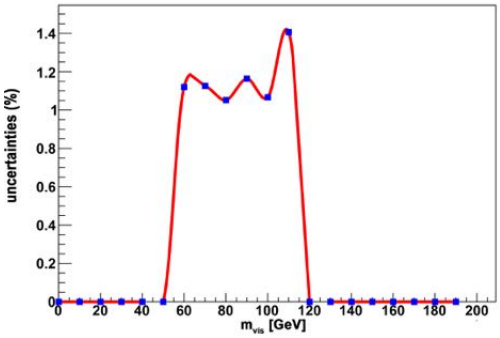

(b) m_{vis} α_s uncertainty $\mu\tau$ channel

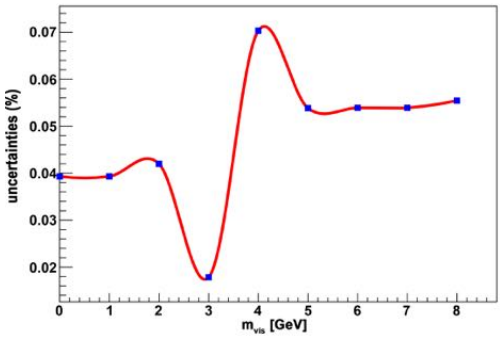

(c) cuts α_s uncertainty $e\tau$ channel

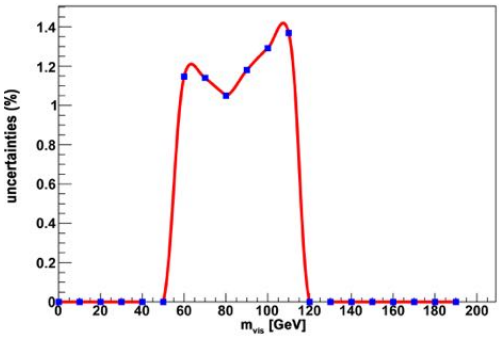

(d) m_{vis} α_s uncertainty $e\tau$ channel

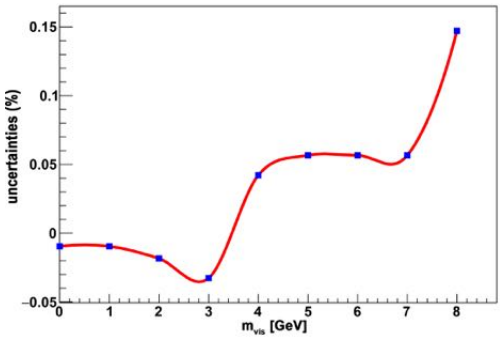

(e) cuts α_s uncertainty $\tau\tau$ channel

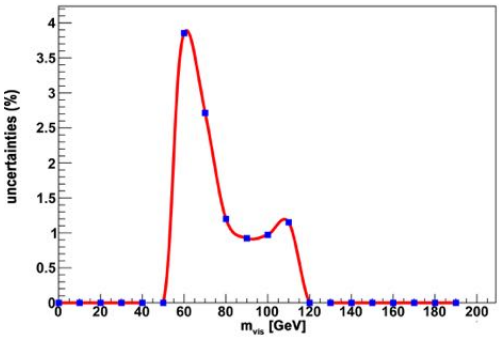

(f) m_{vis} α_s uncertainty $\tau\tau$ channel

Figure 14: α_s uncertainties for cuts (left column) and m_{vis} (right column) for the three decay channels.

7. Uncertainties in the $H \to \tau\tau$ decay mode

In this section this thesis moves from $Z \to \tau\tau$ analysis to $H \to \tau\tau$ analysis. The two production channels in question are the vector boson fusion (VBF) and the gluon-gluon fusion (ggF). Both processes where discussed in section 3.1. The samples were created using a combination of both the POWHEG and Pythia event generators. On the following pages a new preselection is introduced and the cuts are subject to both the new preselection and the preselection used in the previous section (also see section 6.1). After these procedures in section 7.4 additional cuts are made for better background estimation.
Finally this section provides so-called ratio plots to display different observables and their uncertainties. It consists of a histogram which is filled with the distribution of all 100 sets of Monte Carlo PDF sets. Underneath each histogram a graph shows the PDF uncertainties compared to the statistical uncertainties of the distribution to get a glimpse at the magnitude and relation between both uncertainties.

7.1. Preselection

The following preselection will be referred to as preselection 2 and is applied in the second part of this section's cut analysis.

0. Initial number of events going into the preselection.
1. **Decay mode**: Demanding a reconstructed decay mode compatible with a hadronic τ lepton decay.
2. **Isolation 1**: Demanding an isolated first lepton (electron, muon or hadronic τ decay).
3. **Isolation 2**: Demanding an isolated hadronic τ decay (very tight isolation for events of the $\tau\tau$ channel and tight isolation for $\mu\tau$ and $e\tau$).
4. **Lepton veto**: A discriminator against electrons and muons reconstructed as a (hadronically decayed) τ lepton.
5. **Third lepton veto**: The event must not contain a third reconstructed lepton.
6. **Dimuon/electron veto**: No second electron or muon reconstructed.
7. **Transverse mass**: Transverse mass of the W candidate built from a light lepton and E_T^{miss} must be smaller than 40 GeV.

8. **Visible mass**: m_{vis} must lie between 100 and 150 GeV.

7.2. Results for Vector Boson Fusion (VBF)

This sample as discussed describes vector boson fusion, the process in which two massive vector bosons ($W^{\pm}$ or Z) emitted by quarks fuse together to form a Higgs boson. 1 496 072 events were generated by the combined POWHEG and Pythia event generators. In this section two different cuts with different preselections will be executed to give the possibility to determine if the change of selection criteria or its chronological order has any effect on the efficiencies or the PDF uncertainties.
Both cuts and their corresponding uncertainty calculations are also visualized in the graph in figures 15 and 16

7.2.1. Cuts and Uncertainties under preselection 1

Table 5 gives an overview of the single values after each cut:

	$\mu\tau$	$e\tau$	$\tau\tau$
0	0.07	0.04	0.016
1	0.07	0.04	0.016
2	0.068	0.045	0.014
3	0.033	0.021	0.0064
4	0.022	0.012	0.003
5	0.022	0.012	0.003
6	0.022	0.012	0.003
7	0.022	0.011	0.0029
8	0.021	0.011	0.0029

Table 5: Efficiencies (number of events passed divided by the initial total number of events) after every cut for every decay channel.

The PDF uncertainties are generally smaller than for the Drell-Yan samples with values of 0.2 to 0.25%. The last cut shows a peak of 0.4%. Scale uncertainties lie between 0.1 and 0.4% with fluctuations around cut no. 3 and 8. The graph for the uncertainties can be seen in figure 15

7.2.2. Cuts and uncertainties under preselection 2

Table 6 shows the efficiencies for cuts with the preselection 2.

	$\mu\tau$	$e\tau$	$\tau\tau$
0	0.07	0.046	0.016
1	0.07	0.046	0.016
2	0.068	0.045	0.014
3	0.067	0.045	0.013
4	0.033	0.022	0.006
5	0.022	0.012	0.003
6	0.022	0.012	0.003
7	0.022	0.012	0.0029
8	0.022	0.011	0.0029

Table 6: Efficiencies (number of events passed divided by the initial total number of events) after every cut for every decay channel.

The change of the preselection shows almost no change in the calculation of the uncertainties, as witnessed in figure 16.

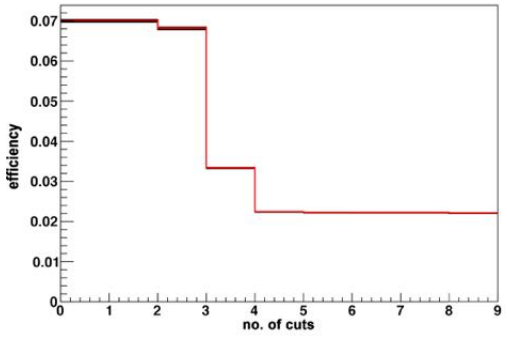

(a) cuts in $\mu\tau$ decay channel

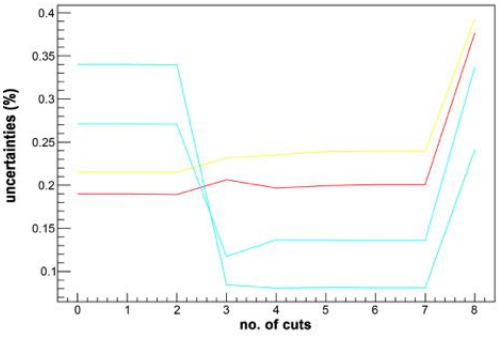

(b) $\mu\tau$ decay channel uncertainties

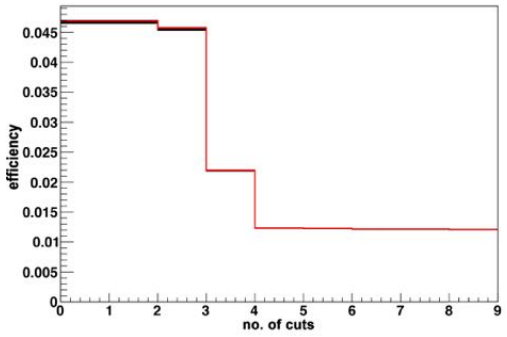

(c) cuts in $e\tau$ decay channel

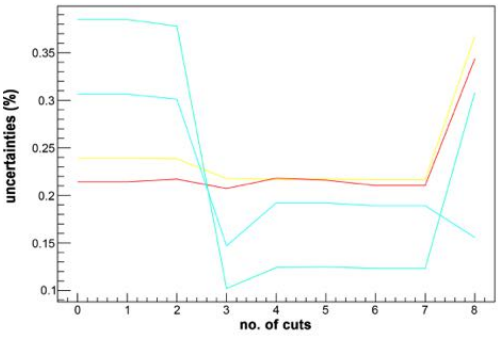

(d) $e\tau$ decay channel uncertainties

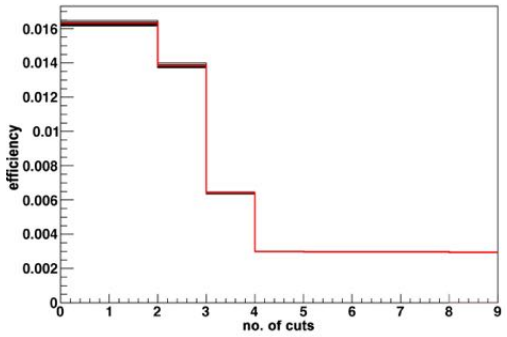

(e) cuts in $\tau\tau$ decay channel

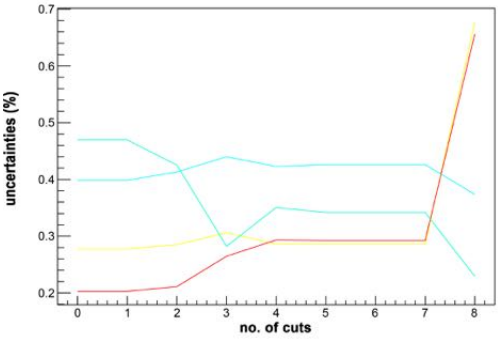

(f) $\tau\tau$ decay channel uncertainties

Figure 15: VBF sample cuts for every decay channel using preselection 1. All 100 sets are plotted on top of each other (the central value is highlighted in red). *Left column*: histogram of efficiency development after every cut. *Right column*: corresponding uncertainties(red: SD; yellow: CL; cyan/teal: scale min/scale max).

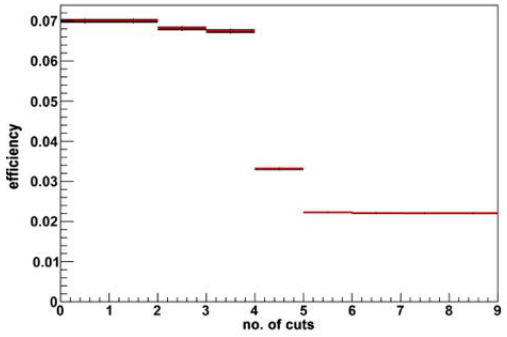

(a) cuts in $\mu\tau$ decay channel

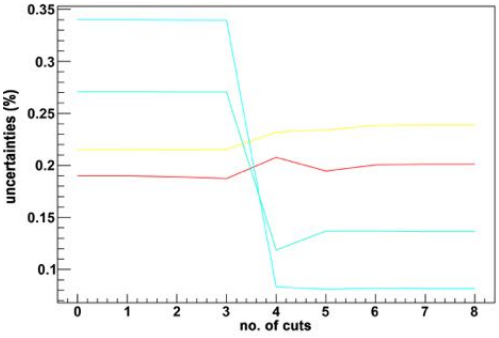

(b) $\mu\tau$ decay channel uncertainties

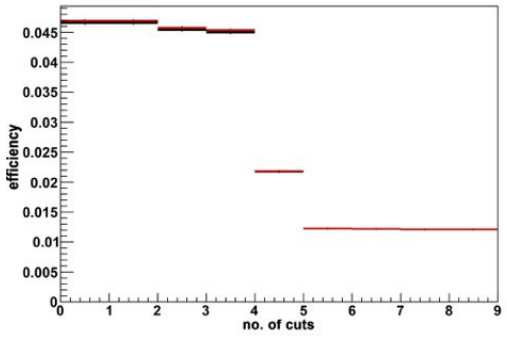

(c) cuts in $e\tau$ decay channel

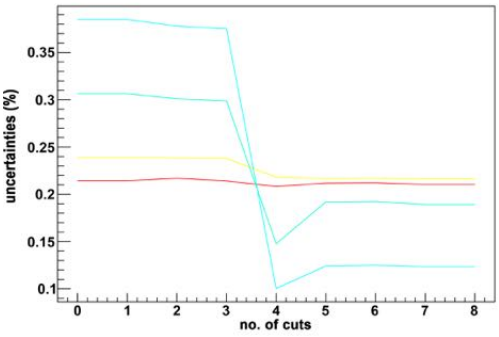

(d) $e\tau$ decay channel uncertainties

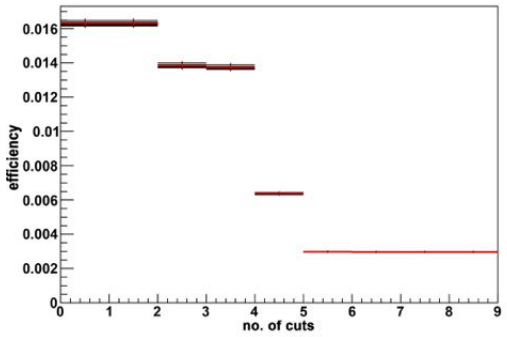

(e) cuts in $\tau\tau$ decay channel

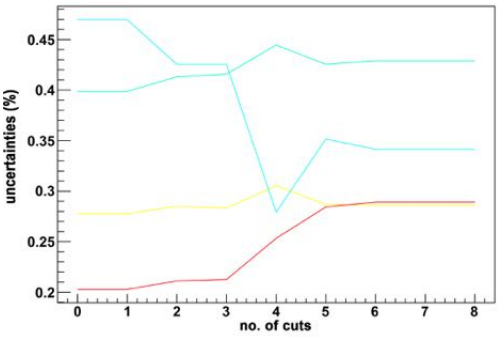

(f) $\tau\tau$ decay channel uncertainties

Figure 16: VBF sample cuts for every decay channel using preselection 2. All 100 sets are plotted on top of each other (the central value is highlighted in red). *Left column*: histogram of efficiency development after every cut. *Right column*: corresponding uncertainties(red: SD; yellow: CL; cyan/teal: scale min/scale max).

7.3. Results for Gluon Gluon Fusion (ggF)

This section covers the so-called gluon gluon fusion (ggF), the process in which a Higgs boson can be produced through gluons. 1 499 028 total events were simulated by the POWHEG and Pythia event generators. Both preselection 1 and preselection 2 are applied in the cuts and are subject to debate in section 8.
As done with the previous sample, all PDF sets were plotted into a histogram and the uncertainty of the resulting distribution was calculated according to the procedure explained in section 5.2. A visual representation of the results can be seen in figure 17 and figure 18 (preselection 2).

7.3.1. Cuts and Uncertainties under preselection 1

First the cuts were executed using the preselection from section 6.1. The results can be viewed in table 7.

	$\mu\tau$	$e\tau$	$\tau\tau$
0	0.12	0.076	0.023
1	0.12	0.076	0.023
2	0.11	0.074	0.02
3	0.06	0.038	0.009
4	0.04	0.021	0.0045
5	0.04	0.021	0.0045
6	0.04	0.021	0.0045
7	0.04	0.021	0.0045
8	0.04	0.021	0.0045

Table 7: Efficiencies (number of events passed divided by the initial total number of events) after every cut for every decay channel.

The uncertainties of said cuts are depicted in figure 17. With PDF uncertainties of 0.4 to 0.6% the ggF sample shows no significant difference to the VBF sample. However the scale uncertainties seem to be higher with ranges of 0.4 to 2% and even 2 to 6% in the $\tau\tau$ channel.

7.3.2. cuts under preselection 2

For the $H \to \tau\tau$ analysis the preselection for the cuts was varied (see section 7.1). Table 8 shows the efficiencies for the new preselection.

	$\mu\tau$	$e\tau$	$\tau\tau$
0	0.048	0.029	0.0076
1	0.048	0.029	0.0076
2	0.046	0.025	0.0065
3	0.046	0.025	0.0065
4	0.027	0.016	0.0033
5	0.019	0.009	0.0015
6	0.019	0.009	0.0015
7	0.019	0.009	0.00151
8	0.019	0.009	0.0015

Table 8: Efficiencies (number of events passed divided by the initial total number of events) after every cut for every decay channel.

In analogy to the previous sections the uncertainties were computed and can bee seen in figure 18 respectively. Here also the PDF uncertainties lie at around 0.4 to 0.6%. Scale uncertainties were calculated as 2 to 3.5%

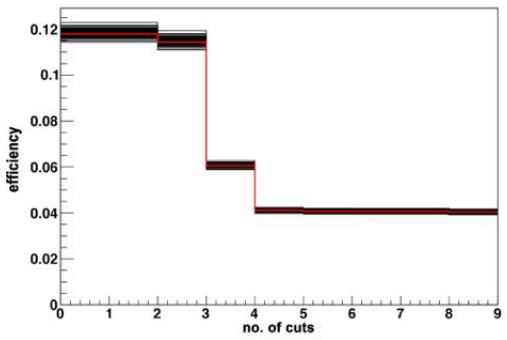

(a) cuts in $\mu\tau$ decay channel

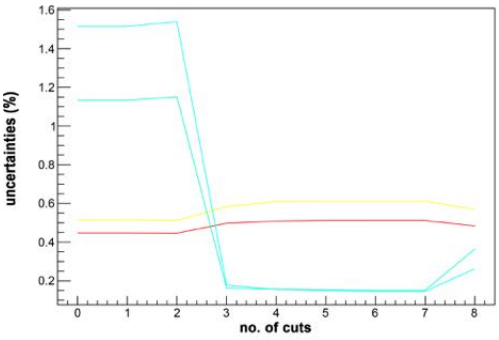

(b) $\mu\tau$ decay channel uncertainties

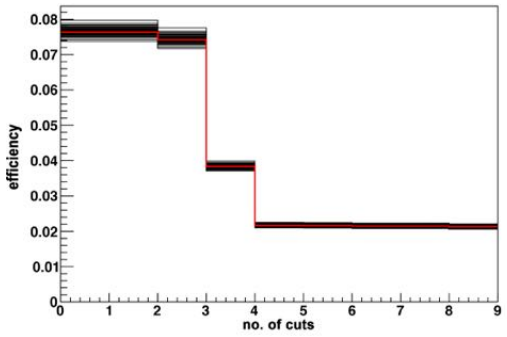

(c) cuts in $e\tau$ decay channel

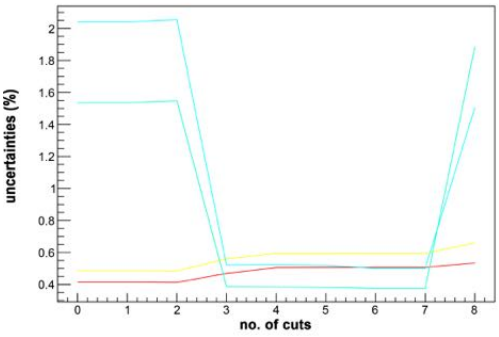

(d) $e\tau$ decay channel uncertainties

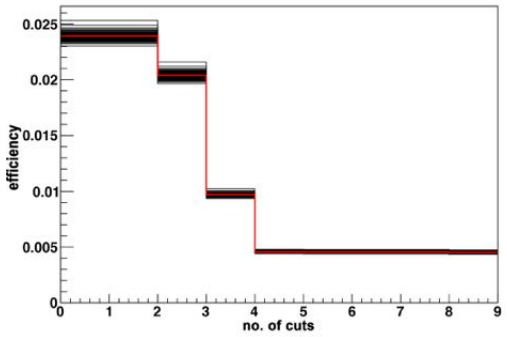

(e) cuts in $\tau\tau$ decay channel

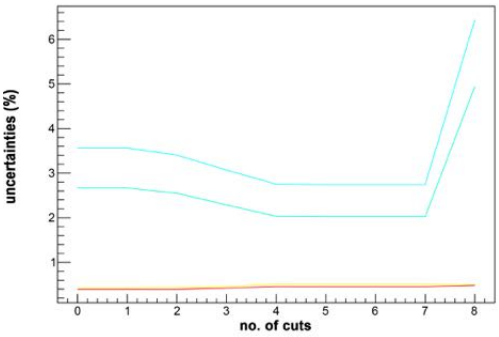

(f) $\tau\tau$ decay channel uncertainties

Figure 17: ggF sample cuts for every decay channel using preselection 1. All 100 sets are plotted on top of each other (the central value is highlighted in red). *Left column*: histogram of efficiency development after every cut. *Right column*: corresponding uncertainties(red: SD; yellow: CL; cyan/teal: scale min/scale max).

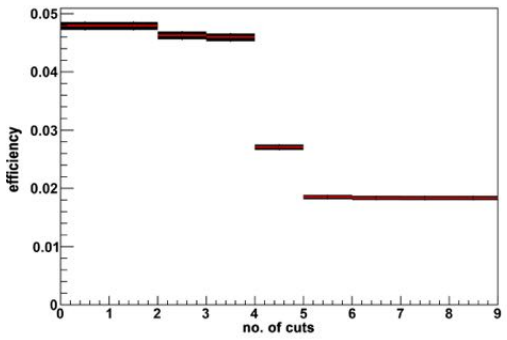

(a) cuts in $\mu\tau$ decay channel

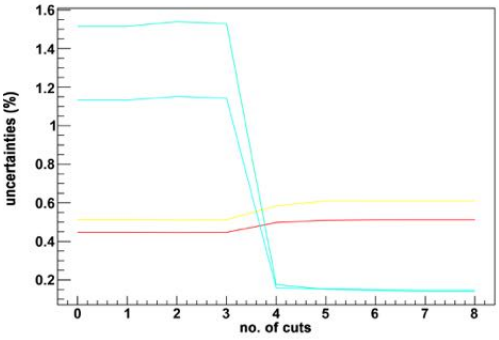

(b) $\mu\tau$ decay channel uncertainties

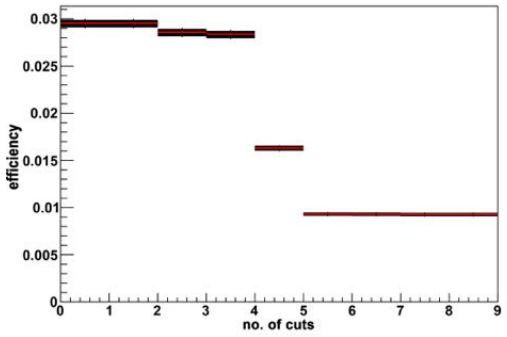

(c) cuts in $e\tau$ decay channel

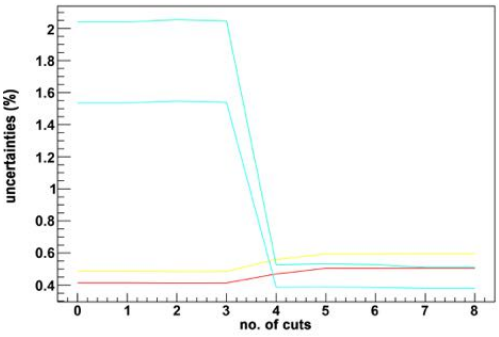

(d) $e\tau$ decay channel uncertainties

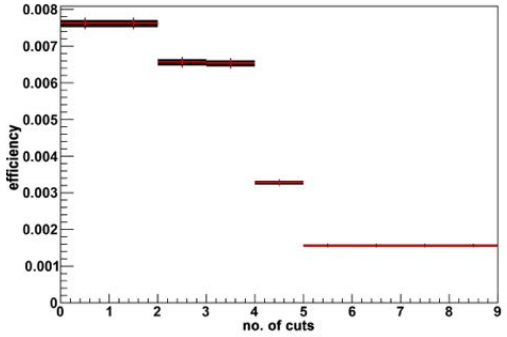

(e) cuts in $\tau\tau$ decay channel

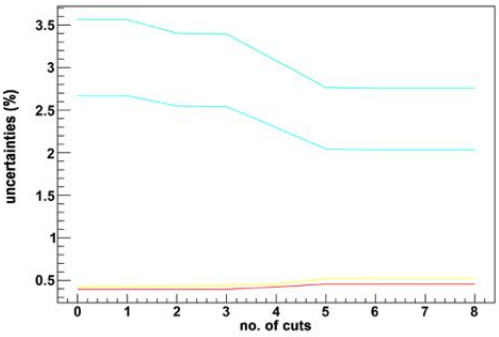

(f) $\tau\tau$ decay channel uncertainties

Figure 18: ggF sample cuts for every decay channel using preselection 2. All 100 sets are plotted on top of each other (the central value is highlighted in red). *Left column*: histogram of efficiency development after every cut. *Right column*: corresponding uncertainties(red: SD; yellow: CL; cyan/teal: scale min/scale max).

7.4. Additional Categories

After variation of the preselection further alterations were made to determine PDF uncertainties and to achieve a better estimation for the signal background.
A new category is defined, which includes very specific conditions each event has to pass to get better estimations for the signal background.

In this section events only pass the cuts if they fulfil the following conditions, which were selected in terms of empirical value and results of previous experiments [1]. Only events with one or two jets will pass:

- Events with 1 jets
  - $p_T^{\tau\tau} > 100GeV$
- Events with 2 jets
  - $\Delta\eta^{jj} > 2.5$
  - $mjj > 300GeV$

If an event contains one jet, then only events with a transverse impulse of more than 100 GeV are allowed. Events with 2 jets may pass when the pseudorapidity between both jets exceeds 2.5 and the combined mass m^{jj} is greater than 300 GeV.

For this additional analysis, a custom preselection was used:

0. **Number of jets**: Event should contain two or more jets with transverse momenta $p_T > 25$ GeV.
1. **Decay mode**: Demanding a reconstructed decay mode compatible with a hadronic τ lepton decay.
2. **Isolation 1**: Demanding an isolated first lepton (electron, muon or hadronic τ decay).
3. **Visible mass**: m_{vis} must lie between 100 and 150 GeV.
4. **Isolation 2**: Demanding an isolated hadronic τ decay (very tight isolation for events of the $\tau\tau$ channel and tight isolation for $\mu\tau$ and $e\tau$).
5. **Lepton veto**: A discriminator against electrons and muons reconstructed as a (hadronically decayed) τ lepton.
6. **Third lepton veto**: The event must not contain a third reconstructed lepton.

7. **Dimuon/electron veto**: No second electron or muon reconstructed.

8. **Transverse mass**: Transverse mass of the W candidate built from a light lepton and E_T^{miss} must be smaller than 40 GeV.

The following final efficiencies after preselection were computed (table 9):

	$\mu\tau$	$e\tau$	$\tau\tau$
VBA	0.0061	0.004	0.001
ggF	0.0008	0.0004	0.0001

Table 9: Final efficiencies after cuts for ggF and VBA sample under the predefined conditions.

The uncertainty results can be viewed graphically in figures 19 (VBF) and 20 (ggF). While the PDF uncertainties show similar results to the previous analysis for both VBF and ggF sample with values of around 0.2 to 0.5%, the scale uncertainties are significantly higher for the ggF sample with values up to 12%. This could be a consequence of the lower efficiencies than in the previous estimations (figures 17 and 18) by a factor 10. The VBF sample however shows scale uncertainties of 0.3 to 0.5%

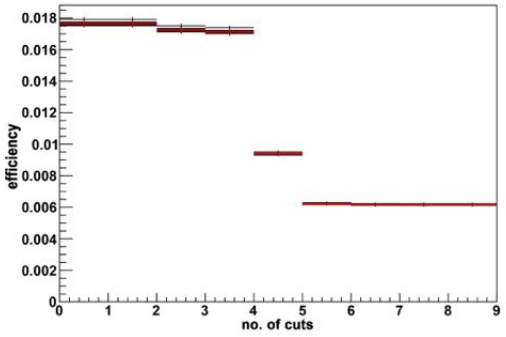

(a) cuts in $\mu\tau$ decay channel

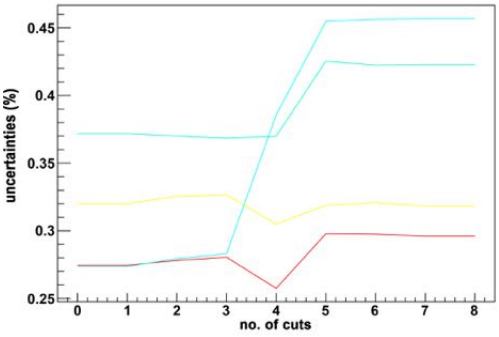

(b) $\mu\tau$ decay channel uncertainties

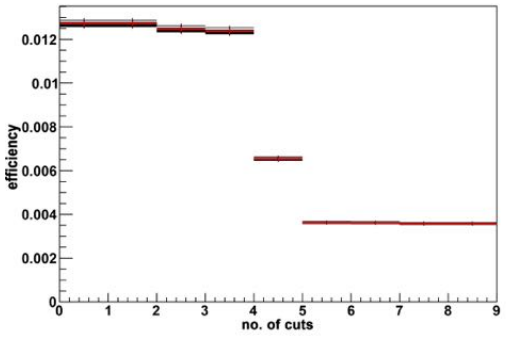

(c) cuts in $e\tau$ decay channel

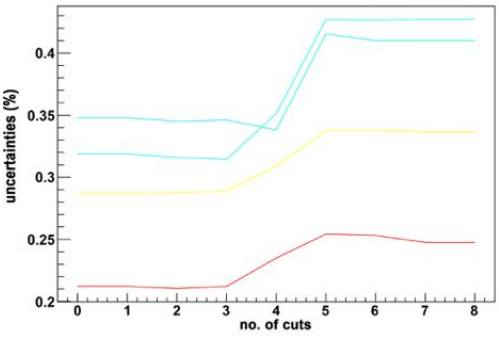

(d) $e\tau$ decay channel uncertainties

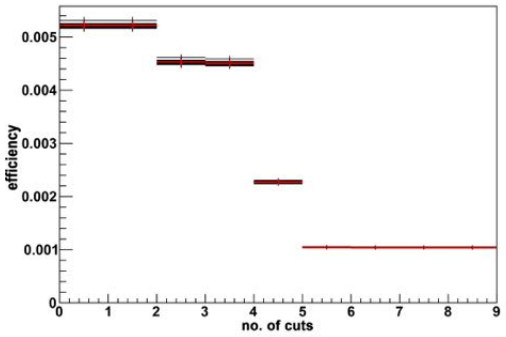

(e) cuts in $\tau\tau$ decay channel

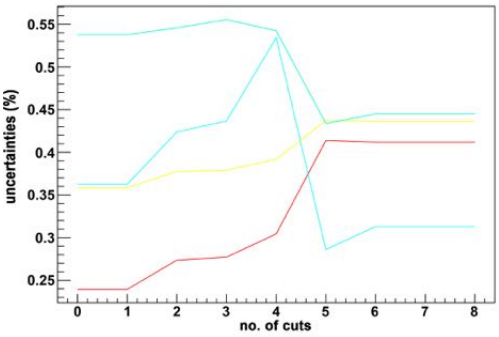

(f) $\tau\tau$ decay channel uncertainties

Figure 19: VBF sample cuts for every decay channel under the precondition defined in section 7.4. All 100 sets are plotted on top of each other (the central value is highlighted in red). *Left column*: histogram of efficiency development after every cut. *Right column*: corresponding uncertainties(red: SD; yellow: CL; cyan/teal: scale min/scale max).

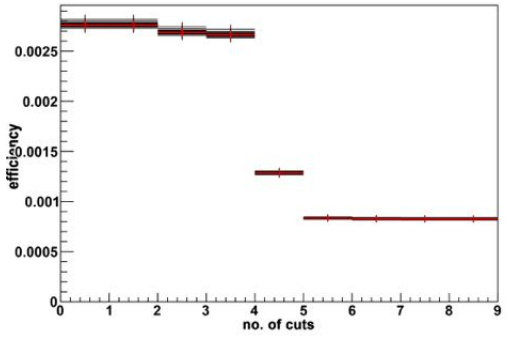

(a) cuts in $\mu\tau$ decay channel

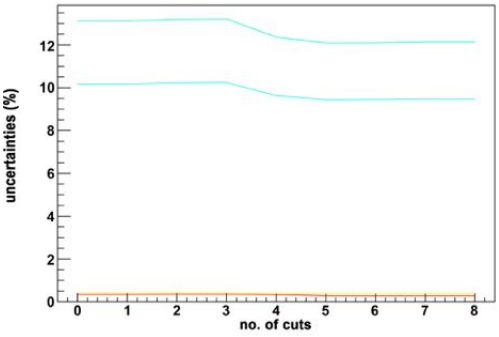

(b) $\mu\tau$ decay channel uncertainties

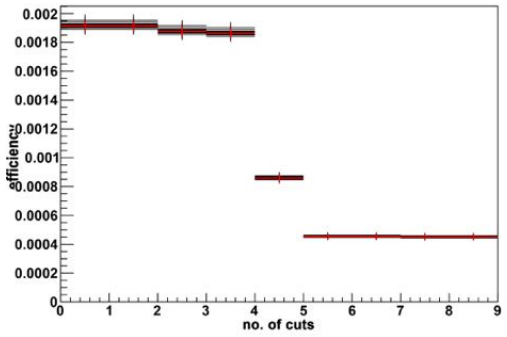

(c) cuts in $e\tau$ decay channel

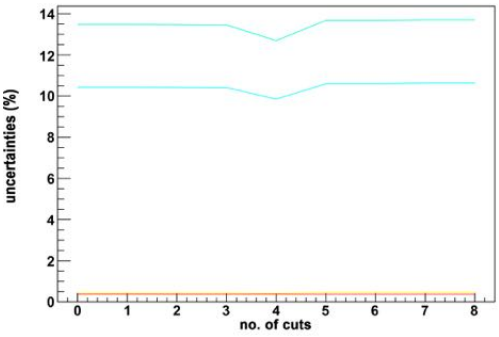

(d) $e\tau$ decay channel uncertainties

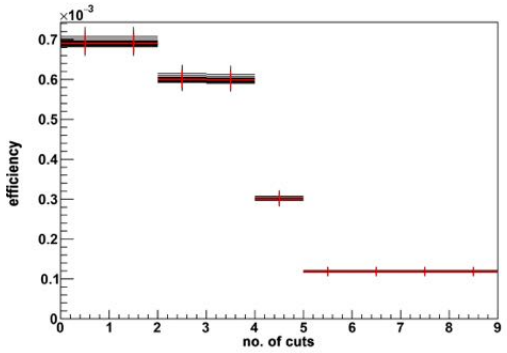

(e) cuts in $\tau\tau$ decay channel

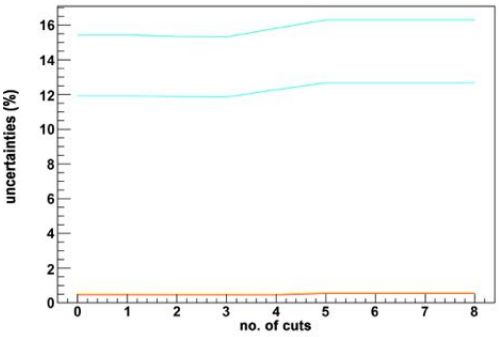

(f) $\tau\tau$ decay channel uncertainties

Figure 20: ggF sample cuts for every decay channe under the precondition defined in section 7.4. All 100 sets are plotted on top of each other (the central value is highlighted in red). *Left column*: histogram of efficiency development after every cut. *Right column*: corresponding uncertainties(red: SD; yellow: CL; cyan/teal: scale min/scale max).

7.5. Ratio plots

Finally some observables are examined in so-called ratio plots. These are, in general, two-part graphs. The upper half shows the histogram of the observables distribution, where all 100 curves (according to all 100 PDF sets) are plotted on top of each other (the central value is displayed in red). The bottom half again shows the ratio of the PDF uncertainties compared to statistical errors. For this all sets were normalised to the value 1 and represented as a dot in every bin. The red dots represent the standard deviation of all dots. The shaded area represents the statistical error (proportional to the square root of the observables value in this particular bin). If the red dot lies within the shaded area, the statistical error is greater than the PDF uncertainties.
This section will examine four different observables:

- the visible mass m_{vis}
- the transverse mass m_T
- the transverse impulse of the τ lepton p_T^τ
- the pseudorapidity between two jets η^{jj}

On the following pages several distributions are plotted. It is only a specific selection of plots, the remaining ones can be viewed in the appendix in section A.

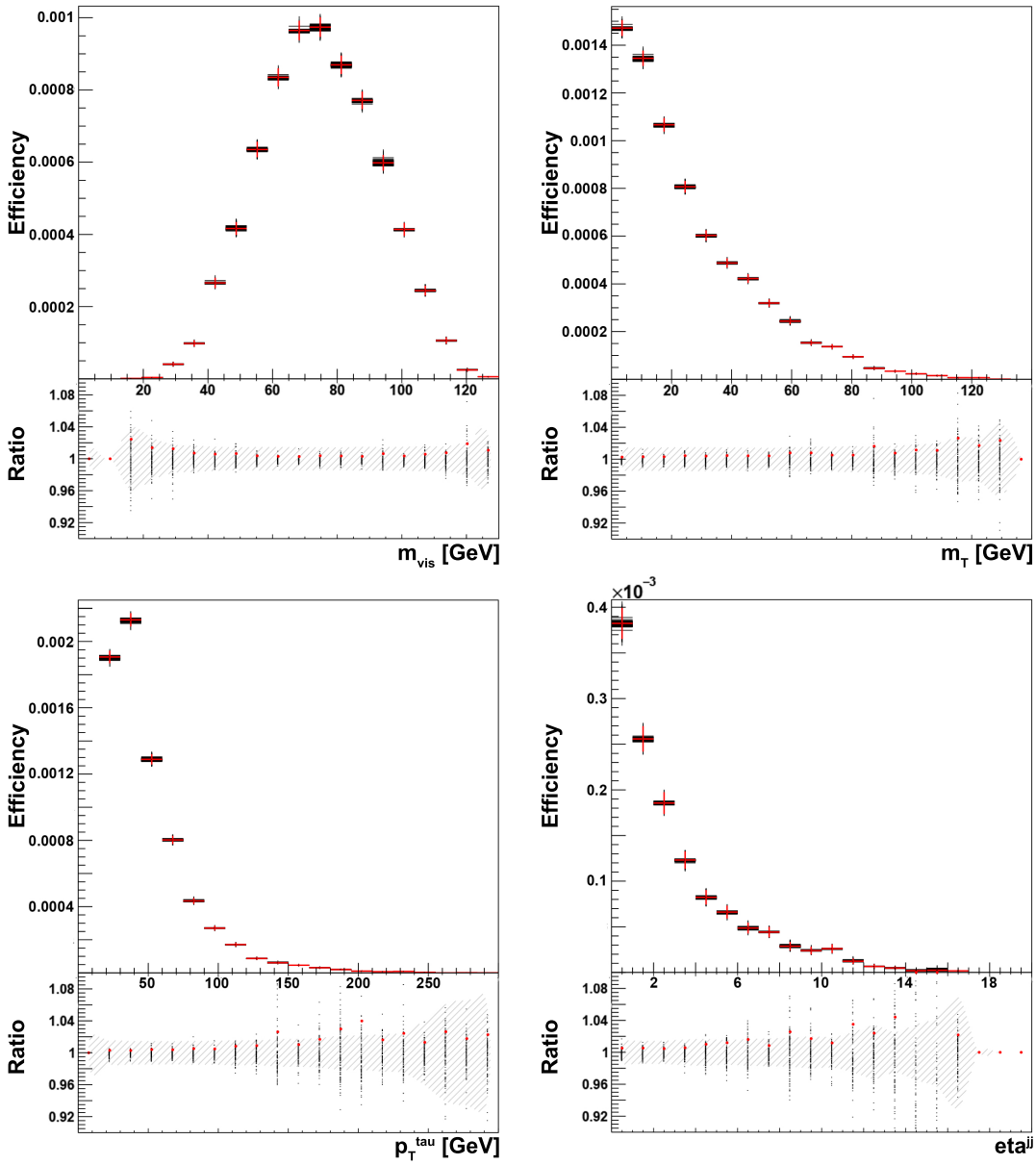

Figure 21: Ratio plots for the VBF sample and the $e\tau$ decay channel in the following order: m_{vis}, m_T, p_T^τ, η^{jj}.

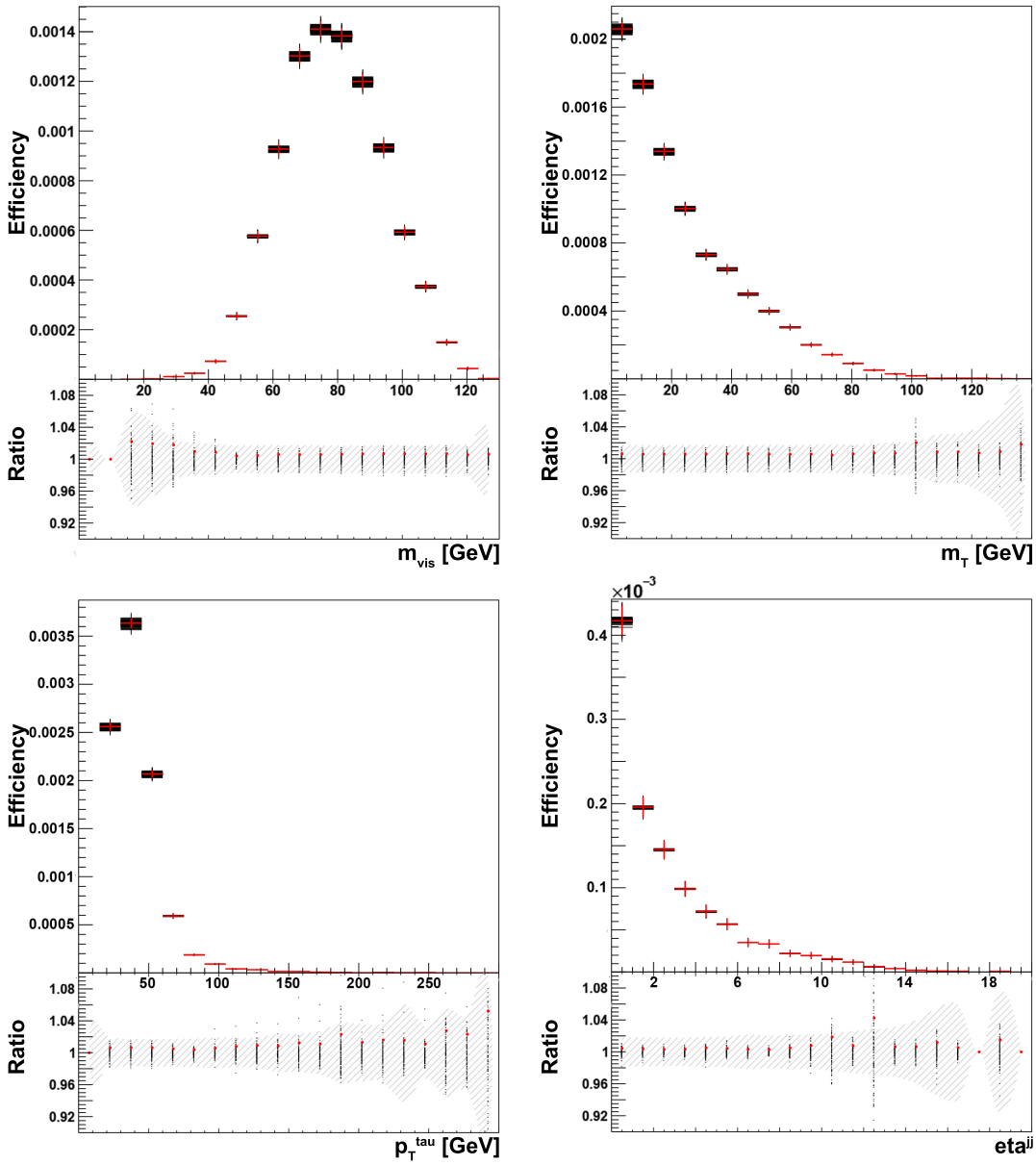

Figure 22: Ratio plots for the ggF sample and the $e\tau$ decay channel, in the following order: m_{vis}, m_T, p_T^{τ}, η^{jj}.

8. Discussion

Applying several different approaches to $H \to \tau\tau$ and $Z \to \tau\tau$ analyses enough information was gathered to reach conclusions about PDF uncertainties.
The PDF uncertainties make up about 0.5 to 1% of the central value.This is true for both $H \to \tau\tau$ and $Z \to \tau\tau$ decays, as with very few exceptions the SD and CL uncertainties do not exceed the 1% threshold. No specific pattern can be detected. Suspicions that uncertainties would peak after cuts with significant decrease in efficiency (like cuts no. 2, 3 and 4 in section 6.1 or no. 3, 4 and 5 in section 7.1) could not be verified.
The α_s uncertainties show the same behaviour, not responding to significant changes in efficiency but rather showing a random pattern around the same value, which lies in the realm of around 0.017%. This indicates that uncertainties associated to varying the α_s parameter are less significant than varying the PDFs.
An attempt to determine the significance of the PDF uncertainties (CL and SD) was made in section 7.5, when histograms of a selection of observables were plotted in comparison to a graph of each uncertainty (normalized) and the statistical error of the distribution. The purpose of this configuration is to compare the PDF uncertainties (red dots) with the statistical error (shaded area) for every bin of the observables histogram. Already a brief examination reveals that for almost every bin the PDF uncertainties lie well within the shaded area. This leads to the conclusion that the PDF uncertainties (in this case SD and CL) are generally smaller than the statistical error, which would mean, that in uncertainty estimations the PDF uncertainties can typically be neglected in comparison to the statistical error.

Looking at the magnitude of the scale uncertainties leads to the conclusion that variation of renormalization and factorization scales have a greater effect on the outcome of the simulation than the variation of PDFs. In $Z \to \tau\tau$ decays, tendentially the scale uncertainties turn out higher with some values crossing the 3% threshold In ggF values up to 6% (section 7.4) or even up to 12% (section 7.3.2) appear. Scale variation impacts ggF more than VBF. This coincides with similar implications made by other research groups in the past [1].

9. Conclusions

Four samples describing three different processes were subject of research in this thesis. The applied procedures resulted in enough data to draw conclusions about the effects of uncertainties in the parton distribution functions as well as the properties of $H \to \tau\tau$ and $Z \to \tau\tau$ decays.

The magnitude of each uncertainty (PDF uncertainties, scale uncertainties, and, in the case of the DY NLO sample, the α_s uncertainties) could be estimated. A representation of the estimated values can be found in table 10, which shows for each sample the interval in which all uncertainties results lie, to give an overview of the magnitude. These values are based on the results of the uncertainties calculations and the recommendations of the PDF4LHC group. These recommendations state that, in the case of larger discrepancies between the calculations, the confidence level calculations shall be used rather than the standard deviation [16].

When looking at the magnitude of the mentioned uncertainties, some conclusions about their significance can be made. The ratio plots show that the statistical error is generally higher than the PDF uncertainties, which suggests that even though the PDF uncertainties may not be negligible, the statistical error is more important in the estimation of uncertainties than the variation of PDFs is. In contrast stand the scale uncertainties. The generally higher values compared to the PDF uncertainties suggest that the variation of factorization and renormalization scales have a significantly greater impact. At last, the α_s uncertainties seem to contribute the smallest share to the uncertainties share since their magnitude is almost smaller by a factor 10.

	PDF uncertainties	Scale uncertainties	α_s uncertainties
DY LO	0.7 - 1.3 %	1.8 - 10.7%	/
DY NLO	0.5 - 0.7 %	0.25 - 3.7 %	0.01 - 0.07 %
VBF	0.18 - 0.67 %	0.08 - 0.47 %	/
ggF	0.4 - 0.62 %	0.13 - 12.7 %	/

Table 10: Estimated uncertainties for all samples. Depicted are the ranges, of the uncertainties.

The acquired data can be used for uncertainty estimation for existing predictions in Higgs boson research.

Appendices

A. Ratio plots

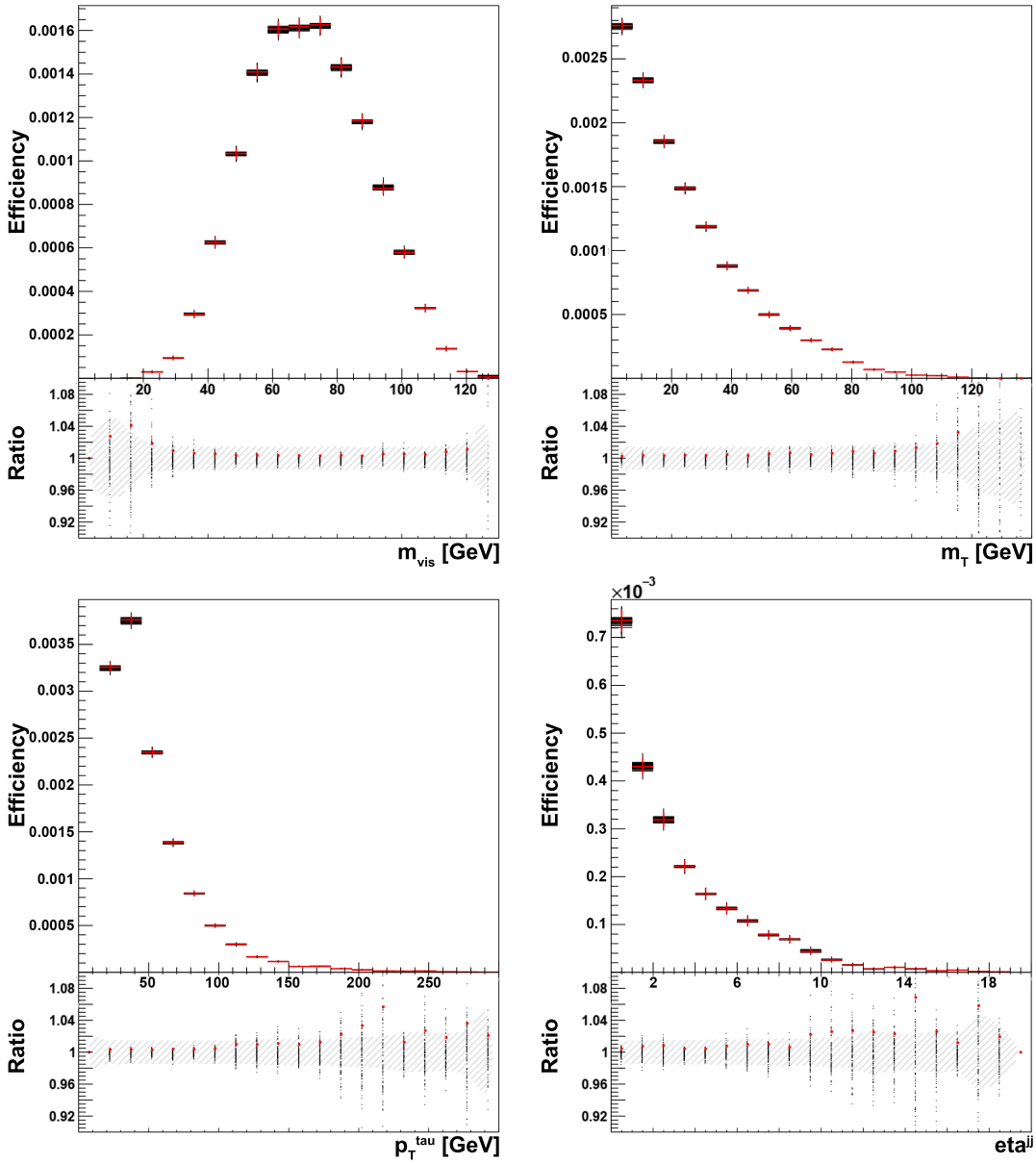

Figure 23: Ratio plots for the VBF sample and the $\mu\tau$ decay channel, in the following order: m_{vis}, m_T, p_T^τ, η^{jj}.

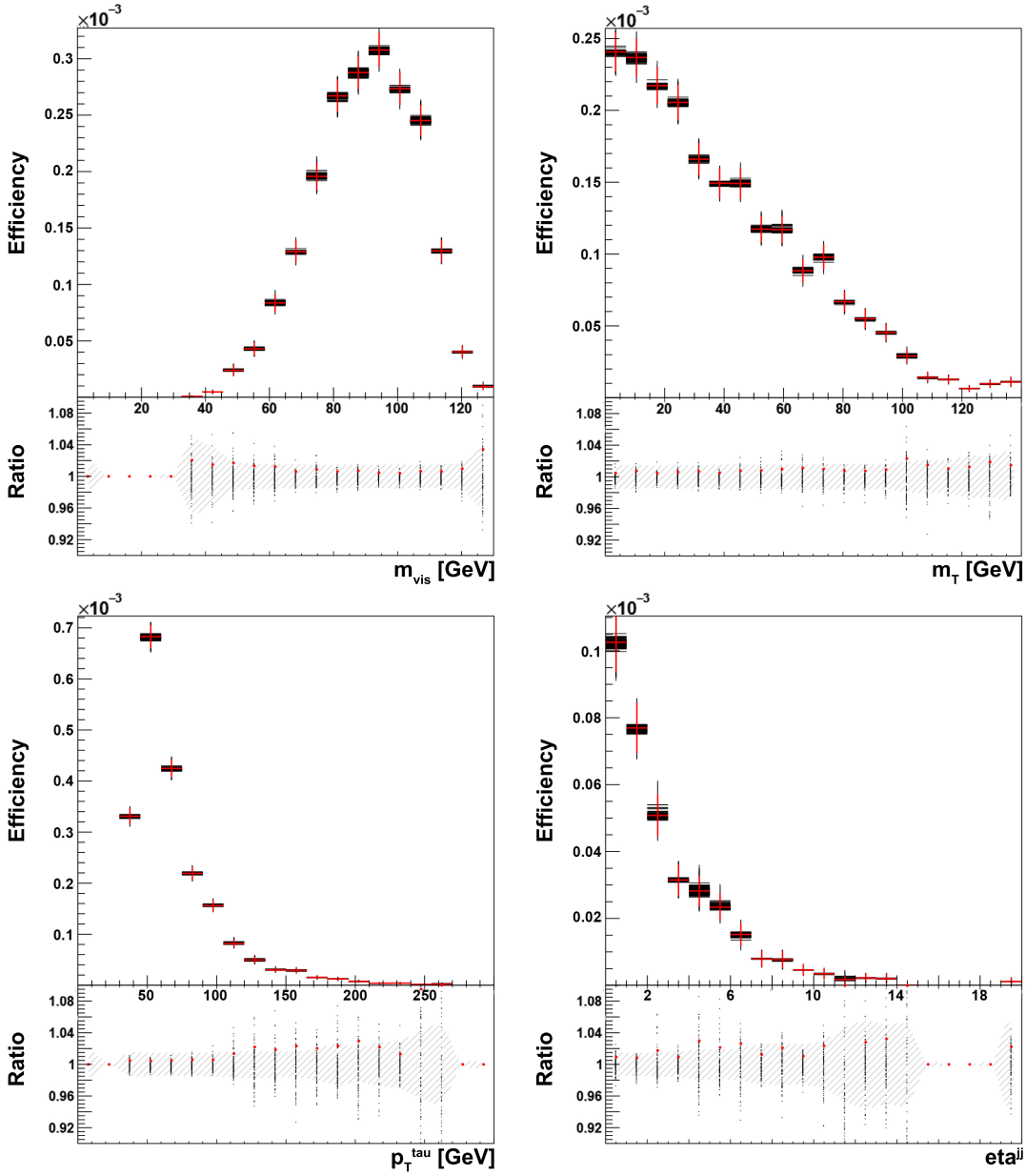

Figure 24: Ratio plots for the VBF sample and the $\tau\tau$ decay channel, in the following order: m_{vis}, m_T, p_T^{τ}, η^{jj}.

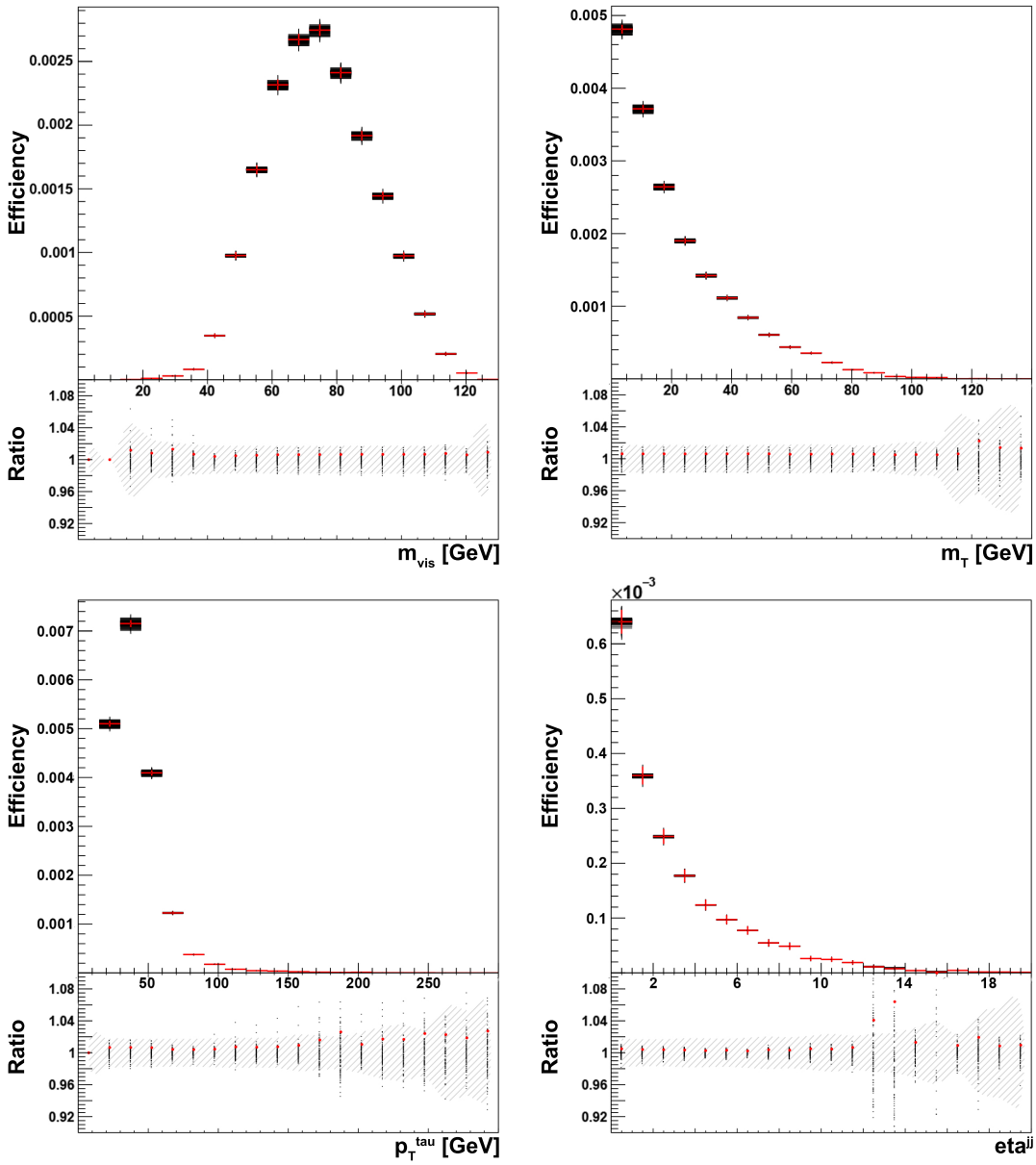

Figure 25: Ratio plots for the ggF sample and the $\mu\tau$ decay channel, in the following order: m_{vis}, m_T, p_T^τ, η^{jj}.

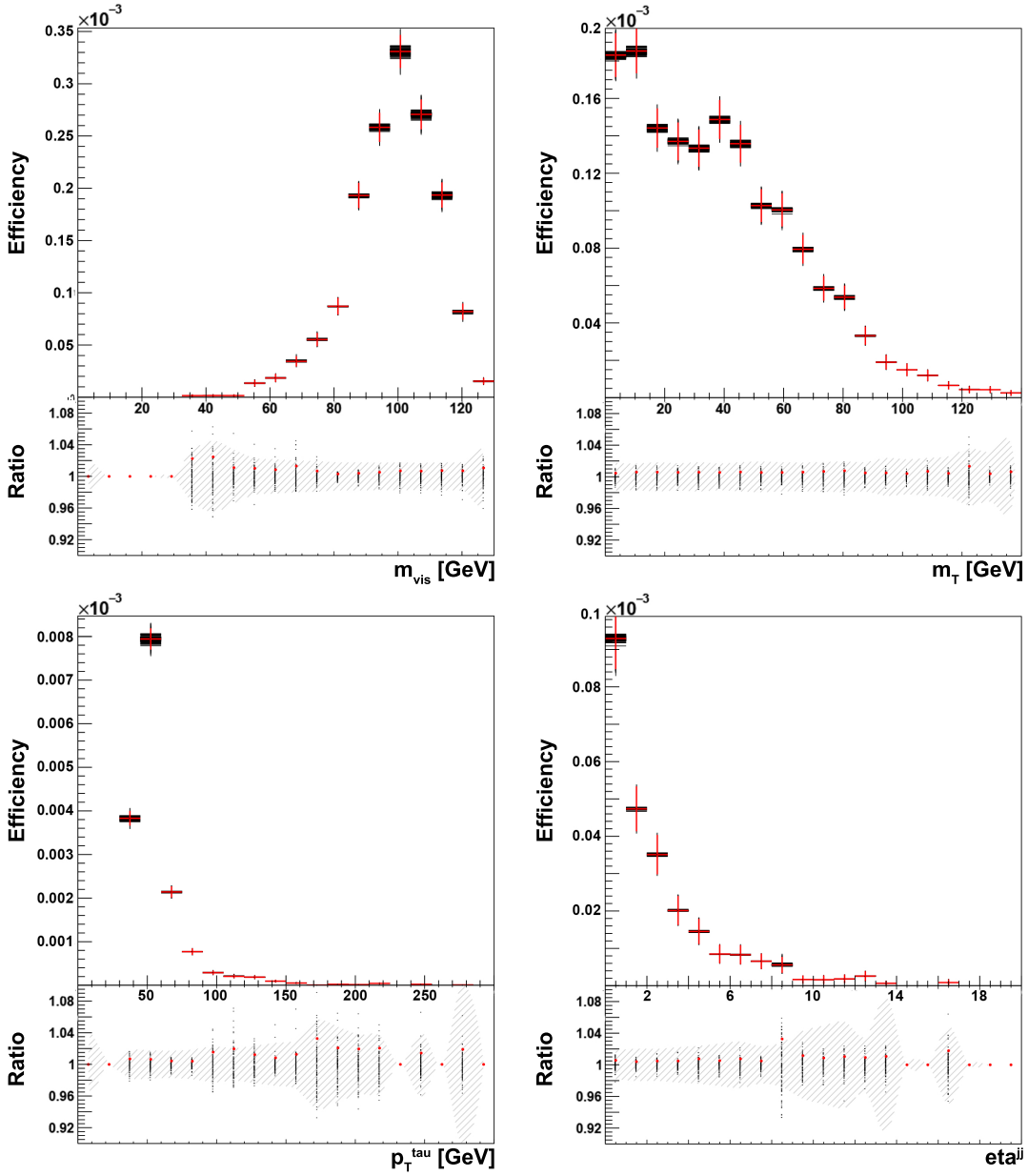

Figure 26: Ratio plots for the ggF sample and the $\tau\tau$ decay channel, in the following order: m_{vis}, m_T, p_T^τ, η^{jj}.

References

[1] J. Howard. *Measurements of the Higgs Boson in the $H \to \tau\tau$ Decay Channel*. PhD thesis, University of Oxford, 2015.

[2] P. W. Higgs. Broken Symmetries and the Masses of Gauge Bosons. *Physical Review Letters*, 13(16), 1964.

[3] M. Carena and et. al. Status of Higgs Boson Physics. *Review of Particle Physics, Chin. Phys. C*, 2014.

[4] M. Grazzini D. de Florian. Higgs production through gluon fusion: updated cross sections at the Tevatron and the LHC. *Phys.Lett.B674:291-294*, 2009.

[5] LHC Higgs Cross Section Working Group. Handbook of LHC Higgs cross sections: 3. Higgs properties. *CERN-2013-004, CERN, Geneva*, 2013.

[6] The ATLAS Collaboration. Combined search for the Standard Model Higgs boson using up to 4.9 fb^{-1} of pp collision data at s=7 TeV with the ATLAS detector at the LHC. *Physics Letters B*, 710(1):49 – 66, 2012.

[7] S. Dittmaier, C. Mariotti, G. Passarino, and R. Tanaka. Handbook of LHC Higgs cross sections: 2. Differential Distributions. *CERN-2012-002*, 2012.

[8] C. O'Luanaigh. LHC to run at 4 TeV per beam in 2012. *CERN Press Office*, 2012.

[9] ATLAS Collaboration. Physics at a High-Luminosity LHC with ATLAS. 25 pages, 18 figures, 8 tables; submitted as input to the Snowmass Community Planning Study 2013. All figures are available at https://atlas.web.cern.ch/Atlas/GROUPS/PHYSICS/PUBNOTES/ATL-PHYS-PUB-2013-007/ ; See paper for full list of authors, July 2013.

[10] J. Haffner. The CERN accelerator complex. 2013.

[11] D. Acosta. CMS Physics Technical Design Report Volume I: Detector Performance and Software. *CERN/LHCC 2006-001*, 2006.

[12] J. Swanson. *Search for a Neutral Higgs Boson decaying to Tau Leptons using CMS at the LHC*. PhD thesis, University of Wisconsin – Madison, 2013.

[13] W. Kilian, J. Reuter, S. Schmidt, and D. Wiesler. An Analytic Initial-State Parton Shower. *Journal of High Energy Physics*, 1204(13), 2012.

[14] T. Sjöstrand, S. Mrenna, and P. Skands. PYTHIA 6.4 physics and manual. *Journal of High Energy Physics*, 2006, 2006.

[15] O. Mattelaer. On the maximal use of Monte Carlo samples: re-weighting events at NLO accuracy. *Eur Phys J C Part Fields*, 76(12): 674(13), 2016.

[16] Jon Butterworth and et. al. PDF4LHC recommendations for LHC Run II. *Journal of Physics G: Nuclear and Particle Physics*, 43(2):023001, 2016.

[17] J. Collins and et. al. Factorization of Hard Processes in QCD. *Adv.Ser.Direct.High Energy Phys.5*, 1-91, 1988.

[18] R. Devenish and A. Cooper-Sarkar. Deep Inelastic Scattering. *Oxford University Press*, 2003.

[19] P. M. Stevenson. Optimized perturbation theory. *Physical Review Letters*, 23(12), 1981.

[20] R. Frederix and et. al. Four-lepton production at hadron colliders: aMC@NLO predictions with theoretical uncertaintiesc. *CERN-PH-TH/2011-250*, CP3-11-32, ZU-TH 19/11, NSF-KITP-11-115, 2011.